HHS Public Access

Author manuscript

Cell. Author manuscript; available in PMC 2023 October 27.

Published in final edited form as:

Cell. 2022 October 27; 185(22): 4153–4169.e19. doi:10.1016/j.cell.2022.09.033.

TREM2 Drives Microglia Response to Amyloid-β via SYK-dependent and -independent Paths

Shoutang Wang[1], **Raki Sudan**[1], **Vincent Peng**[1], **Yingyue Zhou**[1], **Siling Du**[1], **Carla M. Yuede**[2], **Tingting Lei**[1], **Jinchao Hou**[1], **Zhangying Cai**[1], **Marina Cella**[1], **Khai Nguyen**[1], **Pietro L. Poliani**[3], **Wandy L. Beatty**[4], **Yun Chen**[1,5], **Siyan Cao**[1], **Kent Lin**[1], **Cecilia Rodrigues**[6], **Ali H. Ellebedy**[1], **Susan Gilfillan**[1], **Gordon D. Brown**[6], **David M. Holtzman**[5], **Simone Brioschi**[1], **Marco Colonna**[1,7,*]

[1]Department of Pathology and Immunology, Washington University School of Medicine, St Louis, MO 63110, USA

[2]Department of Psychiatry, Washington University School of Medicine, St Louis, MO 63110, USA

[3]Pathology Unit, Molecular and Translational Medicine Department, University of Brescia, Brescia 25123, Italy

[4]Department of Molecular Microbiology, Washington University School of Medicine, St. Louis, MO 63110, USA

[5]Department of Neurology, Knight Alzheimer's Disease Research Center, Hope Center for Neurological Disorders, Washington University School of Medicine, St. Louis, MO 63110, USA

[6]Medical Research Council Centre for Medical Mycology, University of Exeter, Exeter EX4 4QD, Devon, England

[7]Lead Contact

SUMMARY

Genetic studies have highlighted microglia as pivotal in orchestrating Alzheimer's disease (AD). Microglia that adhere to Aβ plaques acquire a transcriptional signature, "disease-associated microglia" (DAM), which largely emanates from the TREM2-DAP12 receptor complex that transmits intracellular signals through the protein tyrosine kinase SYK. The human *TREM2*^{R47H} variant associated with high AD risk fails to activate microglia via SYK. We found that SYK-deficient microglia cannot encase Aβ plaques, accelerating brain pathology and behavioral deficits. SYK deficiency impaired the PI3K-AKT-GSK3β-mTOR pathway, incapacitating anabolic support required for attaining the DAM profile. However, SYK-deficient microglia proliferated

*Correspondence: mcolonna@wustl.edu.

AUTHOR CONTRIBUTIONS

S.W., R.S., Y.Z., S.D., T.L., J.H., Z.C., P.P., W.L.B., Y.C., K.L., M.Ce. and S.B. performed in vitro and in vivo studies. V.P., and K.N. analysed scRNA-seq data. C.M.Y. performed behavioral tests. S.G. prepared some mouse groups. S.W., R.S., Y.Z., Z.C., S.C., and S.B. analyzed data. C.R., G.D.B., and D.M.H., provided critical antibodies. A.H.E., G.D.B., D.M.H., and S.B. provided insightful advice. M.Co. and S.B prepared the manuscript with input from S.W., and V.P. M.Co. conceived and supervised research.

and advanced to an *Apoe*-expressing prodromal stage of DAM; this pathway relied on the adaptor DAP10, which also binds TREM2. Thus, microglial responses to Aβ involve non-redundant SYK- and DAP10-pathways. Systemic administration of an antibody against CLEC7A, a receptor that directly activates SYK, rescued microglia activation in mice expressing the *TREM2*^{R47H} allele, unveiling new options for AD immunotherapy.

Graphical Abstract

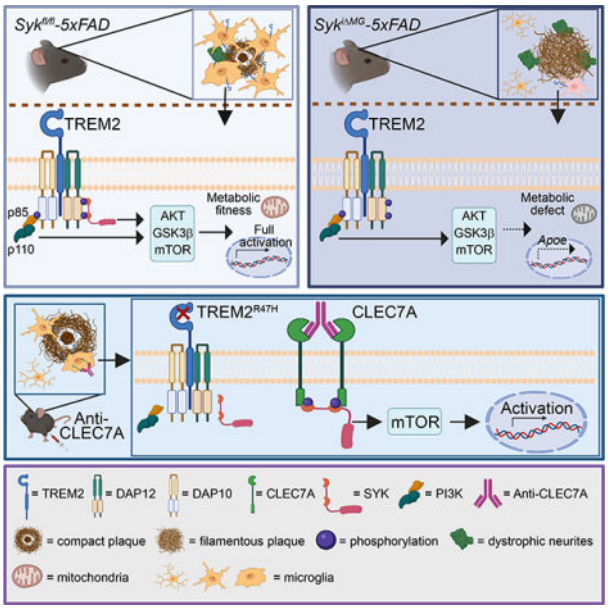

Abstract

Microglia respond to Aβ through the activation of TREM2 mediated Syk and DAP10 signaling mechanisms. Antibody-mediated activation of Syk in mic expressing the Alzheimer's disease associated human TREM2R47H allele rescues microglial activation.

INTRODUCTION

Alzheimer's disease (AD) is the leading cause of late-onset dementia worldwide (2021). AD pathology features extracellular amyloid beta (Aβ) deposition and hyperphosphorylation of intraneuronal Tau, causing neuronal and synaptic loss, ultimately leading to cognitive impairment (Long and Holtzman, 2019). Microglia are professional phagocytes of the central nervous system (CNS) that contribute to CNS development, homeostasis and defense (Prinz et al., 2021; Thion et al., 2018). In response to Aβ pathology, microglia proliferate, associate with Aβ plaques, and acquire an activated transcriptional profile, commonly referred to as disease-associated microglia (DAM) (Keren-Shaul et al., 2017; Friedman et al., 2018; Krasemann et al., 2017; Marsh et al., 2022), Single-cell RNA sequencing (scRNA-seq) has further resolved DAM complexity, identifying four signatures of microglia in amyloid pathology, namely DAM proper (enriched for *ApoE*, *Spp1*, *Clec7a*, *Cd11c*, *Cst7*, *Lpl*), MHC class II (MHCII) microglia (enriched for MHC-II molecules and *Cd74*), type I interferon responsive (IFN-R) microglia (enriched for *Ifitm3*, *Bst2*, *Stat1*), and proliferating

microglia (enriched for *Mki67* and *Top2a*) (Mathys et al., 2017; Sala Frigerio et al., 2019; Ellwanger et al., 2021; Wang et al., 2020). Plaque-associated microglia may help contain Aβ plaques, and delay disease progression (Condello et al., 2015; Wang et al., 2016; Yuan et al., 2016). However, excessive microglia activation may aggravate neuronal damage at later stages of amyloid pathology (Krasemann et al., 2017; Spangenberg et al., 2019; Wes et al., 2016). To comprehend beneficial and detrimental functions of plaque-associated microglia, it is necessary to identify the underlying mechanisms of DAM generation.

The microglial receptor TREM2 binds phospholipids, apoptotic cells, Aβ, and lipoproteins such as ApoE, LDL and HDL (Atagi et al., 2015; Wang et al., 2015; Yeh et al., 2016) (Zhao et al., 2018). TREM2 associates with the transmembrane adaptor DAP12 (Ulland and Colonna, 2018), which recruits spleen tyrosine kinase (SYK) through a cytoplasmic ITAM motif (Chu et al., 1998; Turner et al., 2000; Yao et al., 2019). Blunted microglial responses to Aβ along with impaired acquisition of DAM signature are evident in mice deficient for *Trem2* or expressing the hypofunctional $TREM2^{R47H}$ human variant (Ellwanger et al., 2021; Jay et al., 2017; Lee et al., 2021; Song et al., 2018; Wang et al., 2015). Other than TREM2, there are several immune receptors upregulated in DAM signaling via SYK, including CLEC7A, CD300LB, CD200R4, and the β2 integrin CD11c (Keren-Shaul et al., 2017; Mócsai et al., 2006; Rogers et al., 2005; Wright et al., 2003; Yamanishi et al., 2008). Based on these observations we hypothesized that SYK signaling may play a central role in microglial responses to Aβ.

To test this hypothesis, we crossed the *5×FAD* mouse model of amyloid pathology (Oakley et al., 2006) with $Cx3cr1^{CreERT2} \times Syk^{fl/fl}$ mice lacking *Syk* expression in microglia. Using complementary techniques, we demonstrated that SYK-deficient microglia develop an intermediate activation signature in response to Aβ, but fail to attain a complete DAM phenotype, indicating that microglia require cooperation of both SYK-dependent and -independent pathways to elicit an effective response to Aβ. Furthermore, we demonstrated that immunotherapies boosting SYK through CLEC7A improve microglia activation during Aβ pathology, providing a possible therapeutic avenue for AD.

RESULTS

Conditional *Syk* deletion blunts microglial responses to Aβ pathology and exacerbates plaque deposition

We first tested whether Aβ accumulation activates SYK in microglia. Immunoblot analysis revealed increased SYK phosphorylation in microglia from *5×FAD* mice, whereas the total amount of SYK protein was unchanged (Figure 1A). Next, we crossed $Syk^{fl/fl}$ mice (Saijo et al., 2003) with $Cx3cr1^{CreERT2}$ mice (Yona et al., 2013), which enable inducible deletion of *Syk* in *Cx3cr1* positive cells by administration of tamoxifen (TAM). We refer to these mice as $Syk^{i\Delta MG}$ whereas $Syk^{fl/fl}$ serve as controls. Microglia originate from yolk sac hematopoiesis (Ginhoux et al., 2010; Schulz et al., 2012) and are maintained through self-renewal (Askew et al., 2017; Tay et al., 2017), with no input from circulating monocytes (Goldmann et al., 2013; Gomez Perdiguero et al., 2015). Thus, TAM induction of $Cx3cr1^{CreERT2}$ allows for permanent gene deletion in microglia, while bone marrow-derived monocytes that undergo Cre-mediated recombination are replaced within 4 weeks

due to their constant turnover. We further crossed *Syk*$^{i\Delta MG}$ mice to *5×FAD* mice, which recapitulate features of Aβ pathology characteristic of AD. One-month-old *Syk*$^{i\Delta MG}$-*5×FAD* mice and *Syk*$^{fl/fl}$-*5×FAD* control mice were fed with TAM-containing chow until two months of age and returned to regular chow until 6 or 9 months of age to allow accumulation of Aβ plaques (Figure 1B). Using flow cytometry, we showed that SYK protein was greatly reduced in microglia from *Syk*$^{i\Delta MG}$ mice, whereas monocytes, neutrophils and B cells remained unaffected (Figure S1A, B). Border-associated macrophages (BAMs) exhibited a moderate SYK reduction, consistent with their embryonic origin and slow turnover (Goldmann et al., 2016; Masuda et al., 2022; Utz et al., 2020). However, given the extra-parenchymal localization of BAMs, partial *Syk* deletion in these cells is unlikely to significantly affect parenchymal Aβ pathology. Nine-month-old *Syk*$^{i\Delta MG}$-*5×FAD* mice had markedly less microgliosis and more fibrillar Aβ deposition (Figure S1C–F). In both the cortex and hippocampus, microglia density within a 15-μm radius from plaque borders was significantly reduced in *Syk*$^{i\Delta MG}$-*5×FAD* mice (Figure 1C–E). Likewise, Iba1^{+} methoxy-X04^{+} colocalized staining was diminished in *Syk*$^{i\Delta MG}$-*5×FAD* mice, indicating fewer plaque-associated microglia. This finding was further confirmed by staining for the transcription factor PU.1, which is expressed solely in microglia in the brain parenchyma. A reduced percentage of plaque-associated PU.1^{+} nuclei was apparent in *Syk*$^{i\Delta MG}$-*5×FAD* mice, whereas the density of PU.1^{+} nuclei away from the plaques was unchanged (Figure S1G–I). Of note, no difference in microglia numbers or Iba1 staining was found when comparing *Syk*$^{i\Delta MG}$ and *Syk*$^{fl/fl}$ mice without amyloid pathology (Figure S1J–L). Thus, SYK appears redundant for microglial development and self-renewal in the steady state. Conversely, SYK signaling is required to induce microglia responses to Aβ plaques.

We asked whether SYK deficiency affected microglial phagocytosis. 3D reconstructions of Iba1, CD68, and methoxy-X04 staining revealed Aβ in microglial CD68^{+} phagosomes in both genotypes (Figure 1F). To quantify Aβ uptake, we injected mice intraperitoneally (ip.) with methoxy-X04 and analyzed microglia by flow cytometry. *Syk*$^{i\Delta MG}$-*5×FAD* mice had fewer methoxy-X04^{+} microglia, indicating less Aβ engulfment (Figure 1G, H). To validate this, we assessed pHrodo-labeled A$\beta_{1–42}$ uptake in primary microglia cultures by flow cytometry. Since neonatal mice cannot feed on TAM-containing chow, we cultured microglia from P4 mice with constitutive deletion of *Syk* (*Syk*$^{fl/fl}$ × *Cx3cr1*^{Cre}, referred to as *Syk*$^{c\Delta MG}$) (Yona et al., 2013). SYK-deficient microglia phagocytosed less A$\beta_{1–42}$ than did control microglia (Figure 1I, J). Thus, SYK deficiency affects microglia clustering around Aβ plaques and Aβ phagocytosis.

Lack of SYK in microglia correlates with increased Aβ pathology, neuronal damage and behavioral deficits

We compared *Syk*$^{i\Delta MG}$-*5×FAD* and *Syk*$^{fl/fl}$-*5×FAD* mice for neuronal damage and behavioral alterations. First, we examined brain accumulation of A$\beta_{1–42}$ by immunofluorescence and found that *Syk*$^{i\Delta MG}$-*5×FAD* mice had a significant increase of A$\beta_{1–42}$ deposition at both 6 and 9 months (Figure 2A, B). A$\beta_{1–42}$ is prone to aggregation and adhesion to cell membranes (Masters and Selkoe, 2012; Mucke and Selkoe, 2012), which makes it highly neurotoxic. Thus, we examined the damage of axons and dendrites (collectively neurites) by staining for LAMP1, which labels vesicles accumulating in

dystrophic neurites (Condello et al., 2015). LAMP1 staining volume was significantly amplified in *Syk*$^{i\Delta MG}$-*5×FAD* mice (Figure 2C, D), indicating increased neuronal dystrophy. Similar results were observed by staining for the N terminus of APP, which accumulates in dystrophic neurites (Figure S2A, B). SYK deficiency in microglia also impacted the shape and compactness of Aβ deposits (inert, dynamic, and filamentous plaques) (Figure S2C). *Syk*$^{i\Delta MG}$-*5×FAD* mice had fewer inert plaques at both 6 and 9 months, and more dynamic plaques at 9 months of age (Figure S2D).

Lastly, we performed a battery of behavioral tests. *5×FAD* mice had impaired learning ability in comparison to non-*5×FAD* mice at both 6 and 9 months of age by the end of five days trials in the Morris water maze (Figure 2E, F); no differences were noted between the *Syk*$^{fl/fl}$ and *Syk*$^{i\Delta MG}$ groups at either age (Figure 2F). However, at the memory recall session without a submerged platform, 6-month-old *Syk*$^{i\Delta MG}$-*5×FAD* mice spent significantly less time in the target quadrant than did *Syk*$^{i\Delta MG}$ mice, whereas no difference was found between *Syk*$^{fl/fl}$-*5×FAD* and *Syk*$^{fl/fl}$ mice (Figure 2G). At 9-months, both *Syk*$^{i\Delta MG}$-*5×FAD* and *Syk*$^{fl/fl}$-*5×FAD* groups spent less time in the target quadrant than did either *Syk*$^{i\Delta MG}$ or *Syk*$^{fl/fl}$ mice, with *Syk*$^{i\Delta MG}$-*5×FAD* mice exhibiting the most significant defect (Figure 2G). Latency time to reach the visible platform did not reveal any impairment of visual or swimming ability (Figure S2E). Thus, SYK-deficiency in microglia accelerates memory impairment in *5×FAD* mice.

Mice were also tested at the elevated plus maze, which assesses anxiety levels (Figure 2H). At 6 months, *Syk*$^{i\Delta MG}$-*5×FAD* mice made significantly more entries and traveled longer distances in the open arms than did *Syk*$^{fl/fl}$-*5×FAD* and all non-*5×FAD* mice (Figure 2I, J). At 9 months, however, *Syk*$^{fl/fl}$-*5×FAD* and *Syk*$^{i\Delta MG}$-*5×FAD* behaved similarly: both made significantly more entries and traveled longer distances in the open arms than did non-*5×FAD* mice (Figure 2I, J). All groups travelled comparable total distances, indicating no locomotor impairment (Figure S2F). We conclude that SYK deficiency in microglia exacerbates the $A\beta_{1-42}$ load and neuronal damage, worsening behavioral deficits.

SYK deficiency in microglia dampens mTOR signaling and enhances autophagy

TREM2-DAP12 elicits the PI3K-AKT-mTOR signaling pathway, enhancing anabolic and energy production pathways required for microglia activation (Ulland et al., 2017). Thus, we asked whether SYK acts through a similar mechanism. First, we sorted microglia from *Syk*$^{i\Delta MG}$-*5×FAD* and *Syk*$^{fl/fl}$-*5×FAD* mice (Figure S3A) and performed biochemical analyses. SYK deficiency was associated with reduced phosphorylation of AKT and its targets N-myc downstream regulated 1 (NDRG1) and GSK-3β, which are implicated in mTOR activation, protein synthesis and cell cycle progression (Figure 3A, B). Conversely, ERK was not activated in either genotype (Figure 3B). Microglia from *Syk*$^{i\Delta MG}$-*5×FAD* mice also had significantly reduced mitochondrial mass (Figure 3C, D). Further biochemical analysis was conducted in primary microglia cultures from neonatal mice with a constitutive deletion of *Syk*. Microglia were cultured with or without CSF1-containing medium (LCCM) to evaluate sensitivity to metabolic stress. SYK-deficient microglia had reduced phospho-AKT and the mTOR target phospho-S6 Kinase (S6K) regardless of the presence of CSF1, indicating a metabolic defect (Figure S3B). Thus, SYK-deficient microglia suffer impaired

AKT-mTOR signaling. Concurrently, microglia activated autophagy. The LC3II /LC3I ratio was higher in $Syk^{i\Delta MG}$:5×*FAD* microglia, indicating increased autophagy (Figure 3E). Consistently, immunofluorescence analysis revealed accumulation of $LC3^{+}$ autophagosomes in $Syk^{i\Delta MG}$:5×*FAD* microglia (Figure 3F, G and S3C). Transmission electron microscopy (TEM) corroborated that microglia from $Syk^{i\Delta MG}$-5×*FAD* mice contained abundant multivesicular/multilamellar structures indicative of autophagosomes, which were largely absent in the other genotypes (Figure 3H, I). TEM also showed that $Syk^{i\Delta MG}$:5×*FAD* microglia accumulated lipid-rich vesicles (Figure S3D, E). SYK deficiency may impair cholesterol efflux and lipid catabolism, a defect recently observed in TREM2-deficient microglia (Claes et al., 2021; Nugent et al., 2020; Safaiyan et al., 2021). We conclude that SYK-deficient microglia exhibit metabolic defects during Aβ pathology, such as impaired AKT-mTOR signaling, along with an increase in autophagy.

SYK is required for maintenance of microglial clustering around Aβ plaques

We asked whether SYK deficiency affects microglia fitness when induced during disease progression rather than before its onset. We fed $Syk^{i\Delta MG}$-5×*FAD* and $Syk^{fl/fl}$-5×*FAD* control mice with TAM-containing chow from 4 to 5 months of age (Figure S4A), when mice have already developed Aβ deposits and microgliosis. One cohort of mice was analyzed at the end of TAM treatment (5 months of age), whereas a second cohort was returned to normal chow and analyzed at 9 months of age (Figure S4A). Quantification of plaque-associated microglia in cortex and hippocampus exposed subtle differences between genotypes at 5 months, whereas a significant reduction was observed in $Syk^{i\Delta MG}$-5×*FAD* mice at 9 months of age (Figure S4B–C). Furthermore, analysis of the colocalized Iba1 and methoxy-X04 staining revealed a reduction at both 5 and 9 months of age in cortex and hippocampus (Figure S4B–D). Lastly, we determined whether the total number of microglia was also affected by late *Syk* deletion. Quantification of $PU.1^{+}$ nuclei revealed that microglia numbers were slightly but significantly reduced in $Syk^{i\Delta MG}$-5×*FAD* mice as early as 5 months of age. At 9 months, microglia numbers were elevated in both groups; however, $Syk^{i\Delta MG}$-5×*FAD* mice had significantly fewer microglia than did $Syk^{fl/fl}$-5×*FAD* mice (Figure S4E, F). These results demonstrate that SYK is required for the maintenance of microglial clustering around Aβ plaques after the onset of disease.

SYK deficiency impairs generation of DAM

We examined the impact of SYK deficiency on microglial transcriptome during amyloid pathology by scRNA-seq. Single/live $CD45^{+}$ cells were sorted from $Syk^{fl/fl}$-5×*FAD*, $Syk^{i\Delta MG}$-5×*FAD*, $Syk^{fl/fl}$, and $Syk^{i\Delta MG}$ cortices, and single-cell transcriptomes were generated using the 10x Genomics platform (Figure 4A). After quality control, a total of 89,615 single cells were plotted on uniform manifold approximation projection (UMAP) dimensions for visualization. Unsupervised clustering revealed a total of 15 distinct clusters across all mice (Figure S5A), which were annotated based on differential expression of known cell type-specific marker genes. The preponderance of cells captured by our scRNA-seq dataset were microglia, with significantly fewer BAMs, monocytes, T cells, B cells, and neutrophils (Figure S5B). None of the genotypes had a significant impact on non-microglial cell types.

We next re-clustered microglia only, resulting in 11 distinct clusters comprising 57,830 cells (Figure 4B and S5C). Based on expression of specific marker genes (Chen and Colonna, 2021), we identified homeostatic (clusters 0, 1, 2, and 7), DAM (cluster 6), MHCII (cluster 8), IFN-R (cluster 4), and proliferating (cluster 9, 10) microglia (Figure 4B and S5C–H). We also detected two clusters of microglia with intermediate signatures between homeostatic and DAM, defined as transitioning microglia (TM1 and TM2, clusters 3 and 5), which may represent prodromal stages of DAM. We next examined the representation of DAM, TM1, TM2, MHCII, IFN-R, and proliferating microglia clusters in each genotype (Figure 4C). Notably, DAM appeared almost entirely represented in $Syk^{fl/fl}$-*5×FAD* mice (93.3%), with a minimal contribution from $Syk^{i\Delta MG}$-*5×FAD* mice (5.6%). MHCII and IFN-R microglia were abundant in $Syk^{fl/fl}$-*5×FAD* mice (38.1% and 43.5% respectively), but less represented in the other groups. All genotypes contributed similarly to cycling microglia, though $Syk^{fl/fl}$ contributed the least and $Syk^{i\Delta MG}$-*5×FAD* the most. Breakdown of TM1 among different genotypes showed that 54% of these cells were present in $Syk^{i\Delta MG}$:*5×FAD* microglia, while relatively small percentages were present in the other genotypes (Figure 4C). Thus, SYK deficiency in the *5×FAD* background mainly affected the generation of DAM. However, TM1 microglia (bona fide prodromal to DAM) were expanded, and microglia cycling was unaffected, in fact elevated. This suggests that a basal microglia response to Aβ pathology is maintained in $Syk^{i\Delta MG}$-*5×FAD* mice, although microglia are not able to fully develop a DAM phenotype.

To validate these findings, we performed immunofluorescence staining for TMEM119 (homeostatic marker), TREM2, CLEC7A, CD11c (DAM markers), and CD74 (MHCII marker). Consistent with transcriptomic data, we found significantly fewer $TREM2^+$ (Figure S6A–C), $CLEC7A^+$ (Figure S6D, E), $CD11c^+$ (Figure 4D, E), and $CD74^+$ microglia (Figure 4F, G) in $Syk^{i\Delta MG}$-*5×FAD* mice, along with increased $TMEM119^+$ microglia (Figure S6D, F). These changes were particularly evident in microglia adjacent to Aβ plaques (Figure S6D), whereas SYK deficiency had little impact on microglia distal to Aβ plaques. The morphology of non-plaque associated microglia was also similar in $Syk^{i\Delta MG}$-*5×FAD* and $Syk^{fl/fl}$-*5×FAD* mice (Figure S6G). Immunofluorescence staining for the proliferation marker Ki67 exposed similar numbers of $Ki67^+$ microglia in $Syk^{i\Delta MG}$-*5×FAD* and $Syk^{fl/fl}$-*5×FAD* mice (Figure 4H, I), corroborating scRNA-seq data. We also delved into the characterization of TM1 cells of cluster 3, which were enriched in $Syk^{i\Delta MG}$-*5×FAD* mice (Figure 4J). Analysis of genes differentially expressed among cluster 3, homeostatic cluster 0, and DAM cluster 6, revealed that cluster 3 expressed higher levels of microglia activation genes (*Apoe*, *Ctsz*, *Ctsl*, and *Lyz2*) than did homeostatic microglia. However, these genes were expressed at lower levels in cluster 3 than in DAM. Conversely, the homeostatic genes *Tmem119*, *P2ry12*, and *Fcrls* were more highly expressed in cluster 3 than in DAM but at lower levels than in homeostatic microglia. DAM also expressed high levels of *Cst7* and *Lpl*, which were not detected in either cluster 3 or cluster 0 (Figure 4K, L). Analysis of the DAM signature among clusters 0, 3 and 6 indicated that cluster 3 occupies a transitional state between homeostatic microglia and DAM (Figure 4M). Gene set enrichment analysis of differentially expressed genes in TM and DAM clusters from $Syk^{i\Delta MG}$:*5×FAD* and $Syk^{fl/fl}$:*5×FAD* microglia showed that metabolic pathways were highly affected by SYK deficiency (Figure S6H, I). We conclude that SYK deficiency and the related metabolic

defect prevent the acquisition of a complete DAM phenotype in response to Aβ pathology. However, SYK deficiency does not restrain microglia proliferation and allows accumulation of a microglial population expressing intermediate levels of both homeostatic and DAM genes that is prodromal to DAM.

SYK- and TREM2-deficient microglia exhibit distinct DAM trajectory defects

SYK is a critical component of TREM2 signaling, but is also required by other receptors (Hamerman et al., 2009; Mócsai et al., 2006). Therefore, we sought to examine how SYK-deficiency impacts microglia activation in comparison with TREM2-deficiency. To do so, we re-clustered our scRNA-seq data of *Syk*$^{i\Delta MG}$*:5×FAD* and *Syk*$^{fl/fl}$*:5×FAD* microglia together with newly generated scRNA-seq data from *Trem2*$^{+/+}$*-5×FAD* and *Trem2*$^{-/-}$*-5×FAD* microglia. We identified 10 clusters recapitulating the same populations described above (Figure 5A, B). Because the MHC-II cluster (cluster 9) contained only 167 cells, this population was excluded from further analyses. We next analyzed the representation of the remaining microglial clusters in each genotype. Compared to their respective controls, both *Syk*$^{i\Delta MG}$ and *Trem2*$^{-/-}$ microglia evinced a decrease in DAM (cluster 4), IFN-R (cluster 5), and TM2 (cluster 6, a DAM prodromal stage), whereas some homeostatic populations were expanded (particularly cluster 2). However, an increase in the TM1 transitional stage (cluster 3) was only evident in *Syk*$^{i\Delta MG}$ microglia (Figure 5C). Moreover, cycling microglia (cluster 8) was depleted *Trem2r*$^{-/-}$, but not in *Syk*$^{i\Delta MG}$ microglia (Figure 5C). Pseudotime trajectory analysis corroborated that the homeostatic population differentiated into three terminal stages (DAM, IFN-R and cycling microglia). TM1 and TM2 stages appeared to precede DAM, but not IFN-R and cycling clusters (Figure 5D). We next considered the distribution of *Trem2*$^{-/-}$ and *Syk*$^{i\Delta MG}$ microglia along these three trajectories. *Trem2*$^{-/-}$ microglia were associated with a complete blockade of all fates. By contrast, *Syk*$^{i\Delta MG}$ microglia were partially inhibited along the DAM trajectory with an arrest at the transitional stage TM1, the IFN-R trajectory was moderately impaired, and no defect was observed in the cycling trajectory (Figure 5E). Thus, unlike *Trem2*$^{-/-}$ microglia, *Syk*$^{i\Delta MG}$ microglia can proliferate and initiate a DAM differentiation program, but are unable to reach a DAM terminal stage, resulting in the accumulation of the prodromal stage TM1 (Figure 5F).

We then assessed the DEGs between these two genotypes along the DAM trajectory. We identified 16 DEGs, including the DAM signature genes *Apoe* and *Fabp5*, which were both reduced in *Trem2*$^{-/-}$ microglia compared to *Syk*$^{i\Delta MG}$ and control microglia (Figure 5G). Focusing specifically on the TM1 cluster, *Apoe* was sharply enriched in *Syk*$^{i\Delta MG}$ microglia, compared to *Trem2*$^{-/-}$ microglia (Figure 5H). Collectively, these data suggest that induction of *Apoe* is TREM2-dependent but SYK-independent, at least in part. Yet, absence of SYK impedes the acquisition of a complete DAM signature. To further corroborate this conclusion, we performed immunofluorescence staining for ApoE on brain sections from all analyzed groups (Figure 5I, J). Both *Trem2*$^{-/-}$*-5×FAD* and *Syk*$^{i\Delta MG}$*- 5×FAD* mice had a reduced percentage of ApoE^{+} plaques compared to respective controls, which is consistent with the significant reduction of DAMs in both genotypes. However, reduction in ApoE^{+} plaques was more significant in *Trem2*$^{-/-}$*-5×FAD* mice than in *Syk*$^{i\Delta MG}$*-5×FAD* mice (−76.2% vs −36.7% respectively) (Figure 5K, L). Moreover, the staining pattern of plaque-associated ApoE in *Syk*$^{i\Delta MG}$*-5×FAD* mice appeared more diffuse than in *Syk*$^{fl/fl}$*-5×FAD*

mice (Figure 5J). This may be due to the defective clustering of $Syk^{i\Delta MG}$ microglia and/or tempered ApoE production. We conclude that Aβ pathology may elicit a TREM2-dependent, yet SYK-independent, pathway in microglia that is sufficient to support both proliferation and advancement to a prodromal stage of DAM, which is demarcated by simultaneous expression of homeostatic genes and *Apoe*.

DAP10 activates microglia independently of SYK

We sought to determine how TREM2 activates microglia independently of SYK. It has been shown that the TREM2-DAP12 complex modulates ERK activation through a pathway independent of SYK (Peng et al., 2010). We asked whether this pathway could induce the large $Apoe^{+}$ TM1 cluster observed in SYK-deficient microglia. To test this, we used DAP12 knock-in mice (known as $Dap12^{K\Delta Y75}$), which harbor a deletion in the cytoplasmic motif of DAP12 that disrupts signaling without affecting pairing with TREM2 and trafficking to the cell membrane (Tomasello et al., 2000). We then crossed $Dap12^{K\Delta Y75}$ with $5\times FAD$ mice and analyzed microglia from 6-month-old $Dap12^{K\Delta Y75}$-$5\times FAD$ and $5\times FAD$ mice by scRNA-seq. $Dap12^{K\Delta Y75}$:$5\times FAD$ microglia evinced a phenotype mirroring that of microglia in $Syk^{i\Delta MG}$:$5\times FAD$ mice - i.e. preserved cycling microglia and accumulation of $Apoe^{+}$ TM1 population (Figure 6A, B). Biochemical analysis of bone marrow-derived macrophages (BMDM) from $Dap12^{K\Delta Y75}$, $Trem2^{-/-}$ and $Syk^{c\Delta MG}$ mice showed that lack of either TREM2 or DAP12, but not SYK, impacted ERK activation (Figure 6C), corroborating that the microglia phenotype induced by SYK deficiency is independent of any signal dependent on the TREM2-DAP12 axis.

In addition to DAP12, TREM2 associates with the transmembrane adapter DAP10 (*Hcst*) in BMDM (Peng et al., 2010). DAP10 is similar to DAP12 but lacks a canonical cytoplasmic ITAM. In fact, it contains a cytoplasmic Y-x-N-M motif that directly recruits PI3K and the adapter GRB2 (Lanier, 2009). Thus, we asked whether TREM2-dependent SYK-independent microglia activation requires DAP10. We cultured microglia from $Dap10^{-/-}$ and wild-type neonatal mice pulsed with BrdU and showed that lack of DAP10 impaired microglia proliferation (Figure 6D, E). Biochemical analysis of microglia cultures from $Dap10^{-/-}$, $Trem2^{-/-}$, $Syk^{c\Delta MG}$ and $Syk^{fl/fl}$ mice showed that DAP10-deficiency affected phosphorylation of AKT and its target GSK-3β (Figure 6F). Additionally, $Dap10^{-/-}$ BMDM were more sensitive to the pro-apoptotic effect of the SYK inhibitor BAY61–3606 than wild-type BMDM. The survival defect was completely reversed by a pharmacological inhibitor of GSK-3β, promoting cell survival and proliferation (Eldar-Finkelman, 2002) (Figure 6G, H). Additionally, $Dap10^{-/-}$ BMDM cultured with Aβ oligomers appeared less phagocytic than wild-type BMDM, while SYK inhibition reduced phagocytic capacity in both groups (Figure 6I, J). Comparing $Dap10^{-/-}$, $Trem2^{-/-}$, $Dap12^{K\Delta Y75}$, $Syk^{c\Delta MG}$ and $Syk^{fl/fl}$ BMDM, we confirmed that DAP10 deficiency curtailed phagocytosis, albeit to a lesser extent than did lack of either SYK, TREM2, or DAP12 signaling (Figure 6K). These data demonstrate that DAP10 signaling sustains microglia proliferation, metabolic activation, survival and Aβ phagocytosis independently of SYK, while both pathways are required for full microglia activation.

Anti-CLEC7A improves microglia activation in *5×FAD* mice carrying a TREM2 hypofunctional variant

We previously described a reduced microglia response to Aβ pathology in *5×FAD* mice carrying the human $TREM2^{R47H}$ variant rather than the common variant ($TREM2^{CV}$) (Song et al., 2018). Since the $TREM2^{R47H}$ variant is unable bind ligands and activate SYK, we attempted to rescue SYK activation in this mouse model by engaging an alternative surface receptor that recruits SYK. We chose CLEC7A (DECTIN1), a member of the C-type lectin receptor family that is expressed in neutrophils, dendritic cells, alveolar and peritoneal macrophages (Brown et al., 2002), and is upregulated in microglia during neurodegeneration (Herre et al., 2004; Krasemann et al., 2017; Mass et al., 2017). CLEC7A recognizes β-glucan, a component of the fungal wall, promoting antifungal responses in macrophages (Brown et al., 2002; Underhill et al., 2005). The CLEC7A cytoplasmic domain contains a hemi-ITAM domain that directly recruits and activates SYK upon dimerization (Herre et al., 2004; Rogers et al., 2005; Underhill et al., 2005). To engage CLEC7A in microglia during Aβ pathology, we initially evaluated a recombinant Fc-mutated variant of the anti-CLEC7A monoclonal antibody (mAb) 2A11 (Brown et al., 2002): mAb 2A11 specifically stained microglia cultured from neonatal mice (Figure 7A); moreover, 2A11 mAb-mediated cross-linking of CLEC7A in cultured microglia induced phosphorylation of SYK and S6K (Figure 7B), indicating that this mAb activates CLEC7A in microglia. To test whether CLEC7A engagement can enhance Aβ phagocytosis, $TREM2^{R47H}$-*5×FAD* mice were injected i.p. with a single dose of 2A11 mAb or isotype control. Twenty-four hours after treatment, mice were injected with methoxy-X04 and microglia were analyzed by flow cytometry. More methoxy-$X04^{+}$ microglia were found in the 2A11 mAb- than in the control mAb-treated group, indicating increased Aβ uptake (Figure 7C, D). We next mimicked short-term treatment by injecting $TREM2^{R47H}$-*5×FAD* mice i.p. with mAb 2A11 or isotype control for 10 days. Twenty-four hours after the final injection, mice were analyzed by imaging (Figure 7E). Mice receiving the 2A11 mAb exhibited a significant increase of Iba1 (Figure 7F, G) and CD11c staining (Figure 7H, I), indicating more robust microglia activation. Increased expression of *Itgax* (encoding CD11c) was validated by RT-PCR in brain lysates (Figure 7J). Although short-term treatment did not affect the overall $Aβ_{1–42}$ load in cortex and hippocampus (Figure S7A, B), 2A11 mAb -treated mice had fewer filamentous plaques and more dynamic and inert plaques than did control mice (Figure S7C, D). Thus, CLEC7A engagement in microglia with hypofunctional TREM2 can, at least, partially rescue microglial responses to Aβ (Figure 7K). Lastly, we mined published snRNA-seq data of human AD and age matched controls for expression of *SYK* and *CLEC7A* mRNA using *TREM2* for comparison (Zhou et al., 2020). We confirmed that *SYK* and *CLEC7A* are highly expressed in human microglia from both AD and control subjects (Figure 7L). Thus, the CLEC7A-SYK pathway in microglia might be a potential therapeutic target for AD.

DISCUSSION

This study demonstrates that SYK signaling is a central node in microglia responses to Aβ pathology. Conditional deletion of SYK in microglia prior to or after disease onset dramatically impaired the ability of microglia to encase Aβ plaques, resulting in augmented

Aβ deposition, increased neuronal damage, and worsened behavioral deficits, suggesting that SYK is required for generation and maintenance of microglia responses to Aβ. Mechanistically, SYK deficiency impaired the activation of the PI3K-AKT-GSK-3β-mTOR axis. In parallel, SYK deficient microglia escalated autophagy, which may provide an alternative energetic pathway. Using scRNA-seq, we resolved intermediate and terminal stages of the microglial response to Aβ, showing that SYK-deficient microglia fail to acquire DAM profiles. SYK function in the microglial response to Aβ strikingly mimics that of Drosophila Shark, an analogous non-receptor tyrosine kinase that is recruited to the phagocytic receptor Draper through an ITAM and is required for phagocytosis of neuronal cell corpses by glia (Ziegenfuss et al., 2008). This similarity epitomizes a highly conserved mechanism to clear protein aggregates and cellular debris.

We revealed a notable discrepancy between TREM2-deficient and SYK-deficient microglia at the transcriptomic level. While both SYK and TREM2 deficiencies did impede the generation of DAM, SYK deficiency led to the expansion of a microglia cluster with an intermediate phenotype prodromal to DAM. This suggests that TREM2 activates microglia through a SYK-dependent and a yet unexplored SYK-independent pathway. We provided evidence that TREM2 can sustain SYK-independent microglia activation through DAP10, which directly recruits PI3K (Peng et al., 2010). Accordingly, DAP10 deficiency affected phosphorylation of AKT and GSK-3β and moderated microglia proliferation, survival and phagocytosis.

Lastly, we demonstrated that systemic administration of an agonistic anti-CLEC7A antibody to *5×FAD* mice carrying the hypofunctional *TREM2*^{R47H} variant promotes SYK signaling and improves microglia activation. Since both CLEC7A and SYK are expressed in human microglia, CLEC7A emerges as a potential therapeutic target to boost microglia activation in AD. Thus, therapeutic activation of microglia in AD may be achieved by using agonists for the broad range of receptors that signal through SYK.

Limitations of the study

Our study of SYK-deficient microglia is limited to a prototypic mouse model of Aβ accumulation. While we showed for the first time an impact of SYK and DAP10 signaling on microglia responses to amyloid pathology, how these pathways orchestrate microglia functions remains unclear. Finally, it will be important to determine therapeutic and side effects of the anti-CLEC7A mAb dosing regimen.

STAR + METHODS

RESOURCE AVAILABILITY

Lead Contact—Further information and requests for resources and reagents should be directed to and will be fulfilled by the Lead Contact, Marco Colonna (mcolonna@wustl.edu).

Materials Availability—Materials and reagents used in this study are listed in the Key Resources Table. Reagents generated in our laboratory in this study or previous studies are available upon request.

Data and Code Availability—The accession number for the data reported in this paper is GE0:GSE210258.

EXPERIMENTAL MODEL AND SUBJECT DETAILS

Mice—Mice were of mixed sexes. Mice within experiments were age and sex matched. $Syk^{fl/fl}$- and $Syk^{i\Delta MG}$-5×*FAD* mice were generated by crossing the $Syk^{fl/fl}$-$Cx3cr1^{CreERT2/+}$ mice with $Syk^{fl/fl}$-5×*FAD*. $Syk^{fl/fl}$ mice were also crossed with $Cx3cr1^{Cre}$ mice to ensure constitutive *Syk* deletion, named $Syk^{c\Delta MG}$ in contrast to TAM-inducible $Syk^{fl/fl}$-$Cx3cr1^{CreERT2}$ mice referred to as $Syk^{i\Delta MG}$ mice, that were used for in vitro experiments. $Trem2^{-/-}$, $Dap12^{K\Delta Y75}$, $Dap10^{-/-}$ and $Trem2^{R47H}$-5×*FAD* mice were previously described (Gilfillan et al., 2002; Song et al., 2018; Tomasello et al., 2000; Wang et al., 2015). For generation of bone marrow-derived macrophages (BMDM) 6–12 weeks old mice were used. Primary microglia for culture were isolated from pups at postnatal day 4. Mice used in this study were sacrificed at indicated time points. Mice were housed in the animal facilities of Washington University in St. Louis. All animal experiments were conducted in compliance with Institutional regulations, under authorized protocols # 19–0981 approved by the Institutional Animal Care and Use Committee.

Primary cells—Primary microglia cultures of high purity were generated as previously described (Wang et al., 2015) for Aβ phagocytosis assay, immunoblotting, BrdU proliferation assay and antibody binding assay. In brief, the neonatal mouse brain at P4 was dissected and dissociated by Trypsin (1.67 mg/mL) with Dnase (0.33 mg/mL). The mixed glial culture was resuspended in the complete DMEM medium (supplemented with 1 × GlutaMAX™ supplement, 100 U/mL penicillin-streptomycin, 1 mM sodium pyruvate) containing 10% heat-inactivated fetal bovine serum (FBS) and seeded on PLL-coated T25 flask. From day 5, floating cells (primary microglia) were collected and seeded in 24-well plates at the density of 2×10^5 cells per well in the complete DMEM medium containing 10% heat-inactivated FBS and 10% of L-929 cell conditioned medium (LCCM) for further experiments.

To prepare BMDM for immunoblotting, survival and Aβ phagocytosis assays, bone marrow was collected from femurs and tibias and cells were plated at 5×10^6 cells/100-mm Petri dish in complete RPMI medium (supplemented with 1 × GlutaMAX™ supplement, 100 U/mL penicillin-streptomycin, 1 mM sodium pyruvate) with 10% heat-inactivated FBS and 10% LCCM. Cells were cultured for 5 days before use.

METHOD DETAILS

Mice—For generation of $Syk^{fl/fl}$- and $Syk^{i\Delta MG}$-5×*FAD* mice, 1- or 4-month-old littermates were fed a tamoxifen (TAM) diet for 4 weeks followed by replacement with regular chow. Treated mice were sacrificed at 6-, 9- or 5-, 9-months of age as indicated in the RESULTS. To determine fibrillar Aβ phagocytosis by microglia in vivo, 6-month-old $Syk^{fl/fl}$- and $Syk^{i\Delta MG}$-5×*FAD* mice were intraperitoneally injected with methoxy-X04 (Tocris) at 10 mg/kg in a PBS/DMSO mixture. Mice were sacrificed after 3 hours of injection and brains were made into single-cell suspension. For the short term of anti-CLEC7A antibody treatment, 8-month-old $Trem2^{R47H}$-5×*FAD* mice received intraperitoneal

injection of anti-CLEC7A antibody (2A11), or anti-human ILT1 antibody (Fc mutated, clone 135.5) (Molgora et al., 2020) as a control, for 4 times within 10 days. Mice were sacrificed within 24 hours after the last injection for assessment. For testing the in vivo effect of 2A11 treatment on fibrillar Aβ phagocytosis by microglia *Trem2*^{R47H}*-5×FAD* mice were first injected ip. with a single dose of 2A11 followed by ip. injection of methoxy-X04 after 24 hours.

Flow cytometry—Cells were incubated with Fc block prior to staining. The following antibodies were used in the study: CD45-PE or -APCCy7 (clone 30-F11), CD11b-APC (clone M1/70), Ly6C-APCCy7 (clone HK1.4), Ly6G-FITC (clone 1A8); P2RY12-BV421 (clone S16001E), Syk-PE (clone 5F5), BrdU-PE (Bu20a). Cells, stained with indicated antibodies for 30 min on ice, were acquired (LSR FORTESSA, Canto II, Calibur 3, BD Bioscience) and analyzed using FlowJo software. Cellular mitochondrial mass was assessed by using MitoTracker Green. For antibody binding assay, cells were stained with anti-CLEC7A (2A11) for 30 min on ice followed by a secondary anti-mouse IgG2a-PE staining for 30 min at 4°C. Cells stained by anti-mouse IgG2a-PE only were used as a control. Cell viability was determined by Aqua LIVE/Dead-405 nm staining (Invitrogen) or DAPI, and negative cells were considered viable. Propidium iodide (PI) was used for survival assay. Foxp3/Transcription Factor Staining Buffer Set (eBioscience) was used for intracellular staining.

Cell sorting—Cells from brain were isolated from the indicated animals as previously described (Wang et al., 2015). CD45^{lo}CD11b^{+} microglia or CD45^{+} cells in the brain were fluorescence-activated cell-sorted (FACS Aria II, BD Bioscience) directly into 2%FBS in PBS for TEM or immunoblot lysates or 0.04% bovine serum albumin (BSA) for single-cell RNAseq.

Immunoblotting—Sorted microglia, cultured primary microglia, or BMDM were lysed in cell lysis buffer (Cell Signaling Technology) for 20–30 min on ice. Cell extract was centrifuged at 12000 rpm for 15 min and supernatant was collected and subjected to protein estimation. Equal amount of protein from each sample mixed in 4 × Laemmli sample buffer was loaded on 4–20% mini protein TGX gels from Bio-Rad and run using Tris-Glycine-SDS buffer. Resolved proteins were transferred on PVDF membranes. Membranes were washed using TBST (Tris-buffered-saline with 0.1% tween 20), blocked using 5% BSA or non-fat dried milk and incubated in primary antibody overnight at 4°C. The following primary antibodies were used in the study: anti-phospho Syk (1:500, rabbit monoclonal, Cell Signaling Technology), anti-Syk (1:1000, rabbit monoclonal, Cell Signaling Technology), anti-phospho Akt 473 (1:1000, rabbit monoclonal, Cell Signaling Technology), anti-Akt (1:1000, rabbit monoclonal, Cell Signaling Technology), anti-phospho NDRG1 (1:1000, rabbit polyclonal, Cell Signaling Technologies), anti-NDRG1 (1:1000, rabbit polyclonal, Cell Signaling Technology), anti-phospho GSK3- β (1:1000, rabbit polyclonal, Cell Signaling Technology), anti-GSK3-β (1:1000, rabbit monoclonal, Cell Signaling Technology), anti-phospho ERK (1:1000, rabbit polyclonal, Cell Signaling Technology), anti-ERK (1:1000, rabbit monoclonal, Cell Signaling Technology), anti-phospho S6K (1:1000, rabbit monoclonal, Cell Signaling Technology), anti-S6K (1:1000,

rabbit polyclonal, Cell signaling Technology), anti-LC3 (1:1000, rabbit polyclonal, Cell Signaling Technology), anti-beta-actin-HRP (1:4,000, mouse monoclonal, Santa Cruz Biotechnology). After incubation in primary antibody, membranes were washed and incubated in HRP conjugated secondary antibody for 1 hour at room temperature (RT), washed again and developed using SuperSignal West Pico Plus Chemiluminescent substrate inside Bio-Rad ChemiDoc MP imaging system. Quantification of immunoblotting was performed by ImageJ (National Institutes of Health).

Sample preparation for TEM—Sorted microglia were fixed in 2% paraformaldehyde (PFA)/2.5% glutaraldehyde (Ted Pella Inc.) in 100 mM sodium cacodylate buffer pH 7.2 for 1 hour at RT. Following washes with sodium cacodylate buffer, cells were embedded in 2.5% agarose and post-fixed with 1% osmium tetroxide (Ted Pella Inc.) for 1 hour. After three washes in dH_2O, samples were *en bloc* stained in 1% aqueous uranyl acetate (Electron Microscopy Sciences) for 1 hour. Samples were washed with dH_2O, dehydrated in an ethanol series, and infiltrated with Eponate 12 resin (Ted Pella Inc.). Ultrathin sections (95 nm) were cut with a diamond knife using a Leica Ultracut UCT ultramicrotome (Leica Microsystems Inc.) and counterstained with uranyl acetate and lead citrate. Samples were analyzed and imaged on a JEOL 1200 EX II transmission electron microscope (JEOL USA Inc.) equipped with an AMT 8-megapixel digital camera and AMT Image Capture Engine V602 software (Advanced Microscopy Techniques). Quantitative evaluation was performed by taking random images of 30 cells of comparable size and sectioned through the nucleus (indicating center of cell) and measuring the cross-sectional area using ImageJ. Data was expressed as the total number of a multivesicular/multilamellar structures or lipid droplets per cross-sectional area of cytosol.

Immunofluorescence staining of brain samples—Confocal microscopy analysis was performed as previously described (Wang et al., 2020). Briefly, after transcardial perfusion with ice-cold PBS containing 1 U/ml of heparin, brains were fixed in 4% PFA overnight followed by incubating in 30% sucrose overnight at 4°C before embedding in a 2:1 mixture of 30% sucrose and optimal cutting temperature compound. 40-μm serial coronal sections were cut on a cryo-sliding microtome. Sections were blocked with PBS+5% BSA and permeabilized with 0.5% Triton-X 100 in blocking solution. Primary antibodies were added at indicated combinations overnight at a dilution of 1:1,000 (rabbit monoclonal, Cell Signaling Technology) or 1:500 (goat polyclonal, Abcam) for Iba1, 1:1,000 for CD68 (rat monoclonal, BioLegend), 1:100 for Pu.1 (rabbit monoclonal, Cell Signaling Technology), 1:500 for $A\beta_{1-42}$ (rabbit recombinant monoclonal, Thermo Fisher Scientific) or 1:1,000 for Ap_{1-16} (6E10, BioLegend), 1:1,000 for Lamp1 (rat monoclonal, BioLegend), 1:100 for APP (22C11 mouse mAb, Millipore), 1:50 for LC3-Alexa Fluor® 488 (rabbit monoclonal, Cell Signaling Technology), 1:100 for CD11c (rabbit monoclonal, Cell Signaling Technology), 1:300 for CD74-Alexa Fluor® 647 (rat monoclonal, BioLegend), 1:100 for Ki67 (rabbit polyclonal, Abcam), 1:300 for ApoE (biotinylated HJ6.3, (Xiong et al., 2021), 1:50 for Trem2 (polyclonal sheep, R&D Systems), 1:100 for Tmem119 (rabbit monoclonal, Cell Signaling Technology), 1:50 for Clec7a (rat monoclonal, InvivoGene). Secondary antibodies were added as follows: anti-goat IgG Alexa-Fluor®488 1:1,000 (donkey polyclonal, Abcam), anti-rabbit IgG Alexa Fluor® 555 1:1,000 (donkey polyclonal,

Abcam), anti-goat IgG Alexa Fluor® 647 1:1,000 (donkey polyclonal, Abcam), anti-rabbit IgG Alexa Fluor® 647 1:1,000 (goat recombinant polyclonal, Invitrogen), anti-rat IgG Alexa Fluor®647 1:1,000 (chicken polyclonal, Invitrogen), Streptavidin-Alexa Fluor® 647 1:500 (BioLegend), anti-sheep IgG Alexa Fluor®555 1:1,000 (donkey polyclonal, Abcam) for 1.5 hours at RT. TO-PRO-3 iodide (300 nM; Thermo Fisher Scientific) was used to counterstain for nuclei, and Aβ plaques were labeled with methoxy-X04 (3 μg/ml; Tocris). The respective areas were captured using a conventional fluorescence microscope (Nikon Eclipse 80i microscope) or confocal microscopes (Nikon A1Rsi+ or Zeiss LSM880 airyscan), or a Zeiss Axio Scan 7 Brightfield / Fluorescence Slide Scanner. Images were then processed with Imaris 7.7 (Bitplane).

Microglia clustering analysis—The density of microglial clustering around Aβ plaques within *z* stacks was determined by using the Spots and Surface function of Imaris followed by running an automated scripts in MATLAB as described before (Ulland et al., 2017). Briefly, the Spots function was used to identify microglia within the Iba1 and TO-PRO-3 colocalized channel and the volume as well as location of Aβ plaques was reported by Surface function on methoxy-X04 image data. The density of microglia within 15-μm of plaque surfaces was estimated in MATLAB mathematically. The volumes of dystrophic neurites around plaques were calculated by a similar approach in which the Surfaces function was used to identify the volumes and location of methoxy-X04 as well as Lamp1 or APP positive signals within *z* stacks. Microglial coverage around Aβ plaques was calculated as the total $Iba1^{+}$methoxy-$X04^{+}$ volume divided by the total methoxy-$X04^{+}$ volume. Iba-1 intensity profile was generated by Surface function and the number of microglia was determined by the Spots function of Imaris on Pu.1 image data. Three-dimensional reconstruction of methoxy-X04 and CD68 positive signals was performed by Surfaces function for visualization of Aβ engulfed by microglial $CD68^{+}$ phagosome on the images.

Quantification of Aβ plaques pathology—The measurement of total methoxy-X04 and $Aβ_{1–42}$ area coverage was performed as described before (Wang et al., 2020). Briefly, cortex and hippocampus regions or a similar regions encompassing portions of cortex were drawn in ImageJ from individual image and a threshold in which a fixed intensity was much greater than the mean for the selected region was used for calculating the percentage of area coverage automatically by batch processing in ImageJ. Two or three brain sections per mouse were used for quantification. The plaque load for each mouse was shown as the average of two or three sections. Quantification of Iba1, Tmem119, or Clec7a coverage in the cortex was performed by a similar procedure, with different threshold settings. The conformation of individual plaque in each condition was determined as described before (Wang et al., 2020). Briefly, we evaluated: 1) “inert plaques” made of fibrillar Aβ mostly stained by methoxy-X04; 2) “dynamic plaques” exhibiting a core of methoxy-$X04^{+}$ fibrillar Aβ surrounded by a halo of $6E10^{+}$ non-fibrillar Aβ; 3) “filamentous plaques” with little content of β-sheet structure and branched amyloid fibrils mainly stained with the 6E10 antibody. The proportion of distinct plaque morphology was calculated by normalizing the total number of plaques from each *z*-stack image.

Quantification of microglial activation—For measurement of $CD11c^+$ pixels within $Iba1^+$ pixels, the Spots function on *z*-stack image data was used to conduct the $Iba1^+$ channel. The thresholds for $CD11c^+$ within $Iba1^+$ pixels were determined by visual inspection and used for all images. For each *z*-stack image, the percentages of $CD11c^+$ pixels within $Iba1^+$ pixels were calculated. A similar procedure was used for measurement of percentage of $LC3^+$ or $CD74^+$ microglia over total microglia population. The mean intensity of the TREM2 channel within $Iba1^+$ pixels was exported to Microsoft Excel. A threshold of mean TREM2 intensity was set and simply averaged to obtain the final mean intensity. Sholl analysis of non-plaque associated microglia was perform by ImageJ. Five individuals $Tmem119^+Iba1^+$non-plaque associated microglia in each brain image were analyzed and data from individual cell was averaged to determine the number of intersections in each brain section. Two brain sections from each mouse were calculated and the final results were shown as the average of the number of intersections in each mouse of two genotypes.

Aβ phagocytosis assay in vitro—Human $A\beta_{1–42}$ peptides were aggregated and labeled by pHrodo Red and diluted to a final concentration of 100 μM. 5×10^4 cultured primary microglia or BMDM were seeded overnight into a 96-well plate before adding pHrodo Red labeled $A\beta_{1–42}$ oligomers. Uptake of $A\beta_{1–42}$ aggregates was then captured in a period of 1 or 2 hours by FACS after removing $A\beta_{1–42}$ oligomers from culture media.

In vitro BrdU incorporation—Cultured primary microglia were carefully washed of growth factors and re-plated in a non-tissue culture-treated 96-well plate at 1×10^5 cells per well. After 48 hours cells were pulsed with 10 μM BrdU for additional 48 hours. Cells were detached with 1mM EDTA and BrdU incorporation measured as instructed by the manufacturer (BD Pharmingen BrdU Flow Kit).

Survival assay—To assess cell survival, WT or *Dap10*$^{-/-}$ BMDM were seeded into 96-well plate at 5×10^4/well and cultured with following conditions: 1) 10% LLCM; 2) 0% LLCM; 3) 0% LLCM with 1 μM BAY61–3606 (Syk inhibitor); 4) 0% LLCM with 1 μM BAY61–3606 (Syk inhibitor) and 10 μM SB216763 (GSK-3β inhibitor) 5) 0% LLCM with 10 μM SB216763 (GSK-3β inhibitor) for 48 hours. Frequencies of viable cells were determined by FACS with PI staining.

General design of behavioral tests—All behavioral testing was conducted during the light cycle, by a female experimenter blinded to experimental group. Equipment was cleaned with 2% chlorhexidine diacetate between animals. The order of tests conducted for each cohort were as follows: 1 hour locomotor activity, elevated plus maze, visible platform trials of the water maze, submerged platform trials, and water maze probe trial.

One-hour locomotor activity and open field test.: To evaluate general activity levels mice were evaluated over a 1-hour period in transparent (47.6 × 25.4 × 20.6 cm high) polystyrene enclosures. Each cage was surrounded by a frame containing a 4 × 8 matrix of photocell pairs, the output of which was fed to an on-line computer (Hamilton-Kinder). The system software (Hamilton-Kinder) was used to define a 33 × 11 cm central zone and a peripheral or surrounding zone that was 5.5 cm wide with the sides of the cage being the outermost

boundary. This peripheral area extended along the entire perimeter of the cage. Variables that were analyzed included the total number of ambulations and rearing on hindlimbs, as well as the number of entries, the time spent, and the distance traveled in the center area as well as the distance traveled in the periphery surrounding the center.

Elevated Plus Maze (EPM).: EPM was conducted as previously described (Wozniak et al., 2013). Briefly, a 5 min trial was conducted in a dimly lit room using a standard mouse elevated plus maze from Kinder Scientific (Poway). The maze consisted of a black acrylic surface measuring 5×5 cm and elevated 63 cm above the floor equipped with photo beam pairs. Four arms (35 cm long, 5 cm wide; two open and two with 15 cm high walls) extended from a central area. The MotorMonitor software (Kinder Scientific) quantified beam breaks as duration, distance traveled, entries, and time at rest in each zone (closed arms, open arms and center area).

Morris water maze (MWM).: MWM was conducted as previously described (Wozniak et al., 2004). Briefly, cued (visible platform), place (submerged platform), and probe trials were conducted in a galvanized steel pool, measuring 120 cm in diameter, and filled with opaque water (diluted nontoxic white tempera paint). The PVC escape platform measured 11.5 cm in diameter. A digital video camera connected to a PC computer and the computer software program ANY-maze (Stoelting Co) tracked the swimming pathway of the mouse to the escape platform and quantified path length, latency to find escape platform, and swimming speeds.

On two consecutive days, animals received four cued trials, separated by 1 hour, during which a red tennis ball atop a rod was attached to the escape platform and served as a visual cue. To prevent spatial learning, the escape platform was moved to a different quadrant location for each trial. The mouse was released from the quadrant opposite to the platform location and allowed 60 s to locate the platform. Once the mouse found the platform, it was allowed to remain there for 10 s before being returned to its home cage. Three days following visible platform testing, the cue was removed from the platform, and it was submerged 1 cm under the water for the hidden platform tests. Animals received two blocks of two consecutive trials on five consecutive days, with an inter-trial interval between 30–90 s and approximately 2 hour separating trial blocks. The escape platform remained in the same quadrant location for all trials and distal cues were placed on the walls of the room to support spatial learning. The mouse was released from a different location for each trial on each day. The mouse was allowed 60 s to find the escape platform and allowed to sit on it for 10 s before being returned to its home cage. Visible and submerged platform trials were combined into blocks of two or four trials for analyses, respectively. Following completion of submerged platform trials on the 5th day of training, the escape platform was removed from the pool and one 60 s probe trial was conducted to assess memory retention for the location of the platform.

Single-cell RNAseq—6-month-old of *Syk*$^{fl/fl}$, *Syk*$^{i\Delta MG}$, *Syk*$^{fl/fl}$-*5×FAD* and *Syk*$^{i\Delta MG}$-*5×FAD*, as well as *Trem2*$^{+/+}$-*5×FAD*, *Trem2*$^{-/-}$-*5×FAD* and *DAP12*$^{K\Delta Y75}$-*5×FAD* male mice were sacrificed for the sample preparation. After perfusion with cold PBS, cortices were dissociated, and CD45^{+} cells were sorted using FACS. All CD45^{+} cell libraries

were prepared using the 10x Genomics Chromium Single Cell 3' v3 Gene Expression Kit and sequenced on Illumina NovaSeq.

Anti-CLEC7A-Fc mutated antibody production—Anti-mouse CLEC7A monoclonal antibody (mAb) 2A11 was previously reported (Brown et al., 2002). A DNA fragment encoding heavy chain variable (VH) and CH1 regions was cloned into the pFUSEmIgG2A-Fc1 vector with L234A, L235A, P329G (LALA-PG) mutation, which blocks Fc binding. A DNA fragment encoding the light chain was cloned into Fc-null pFUSE-mIgG2A-Fc1 vector as previously described (Molgora et al., 2020). The heavy chain and light chain plasmids were co-transfected into Expi293F cells (Thermo Fisher Scientific) for expression at mass ratio 1:2. When cell viability was below 50% (5–7 days), the supernatant was collected and filtered with 0.22-μm filters. The antibody was purified with protein A agarose (GoldBio). Final preps were concentrated to about 10 mg/mL into PBS and stored in 80°C for future use.

Stimulation of cultured primary microglia by anti-CLEC7A—Before stimulation, primary microglia were starved for 3 hours in 1% serum RPMI. Cells were incubated on ice for 30 min with 10 μg/ml of anti-CLEC7A or anti-human ILT1 antibody (Fc mutated, clone 135.5) (Molgora et al., 2020) as a control. Cells were then washed 3 times with cold PBS at 4°C and incubated at 37°C for 5 min in the presence of purified goat F(ab')2 anti-mouse IgG(H+L) (15 μg/ml, polyclonal, SouthernBiotech). After stimulation, cells were washed 3 times once again with cold PBS at 4°C and lysed with lysis buffer for the immunoblotting.

qRT-PCR analyses—Total RNA was extracted from cortices of the left-brain hemispheres using miRNeasy Mini Kit (QIAGEN). After cDNA synthesis using a High-Capacity cDNA Reverse Transcription Kit (Applied Biosystems), quantitative PCR was performed using SYBR Green real-time PCR master mix (Thermo Fisher Scientific) and LightCycler 96 detection system (Roche). The reference gene was actin and relative gene expression levels were determined by the ΔΔCt method. Gene expression was considered undetectable if Ct values were >35 cycles.

QUANTIFICATION AND STATISTICAL ANALYSIS

Statistical analysis—All graphs represent the mean of all samples in each group ± SEM as indicated in the figure legends. Statistical analysis was performed using GraphPad Prism software. $P < 0.05$ was considered significant difference between different conditions, determined by a two-tailed unpaired t test, one-way ANOVA with Tukey's multiple comparisons test or two-way ANOVA with Sidak's multiple comparisons test as indicated in the figure legends. P-values in violin plots shown in the Figure 7L were calculated using stat_compare_means() function of ggpubr package (0.4.0) in R, using Wilcox rank-sum test. Quantification of fluorescence microscopy, confocal microscopy and electron microscopy images were performed using Imaris, ImageJ and MATLAB.

Single-cell RNAseq analysis—Cell Ranger Software Suite (v6.0.0) from 10xGenomics was used for sample demultiplexing, barcode processing, and single-cell counting. Cellranger count was used to align samples to the reference genome GRCm39, quantify

reads, and filter reads and barcodes. Only protein-coding genes, with the exception of *Clec7a*, were retained in the analysis. The Seurat (v4.0) package in R (v4.1.0) was used for downstream analysis (Hao et al., 2021). For quality control, cells with mitochondrial content more than 7.5% were removed. Cells with low UMI and gene number per cell were filtered out. Cutoffs for UMI and gene number were empirically determined on the basis of histograms showing cell density as a function of UMI per gene counts. Cutoffs of UMI greater than 2000 and less than 20000, and genes greater than 1000 were applied. Genes expressed in fewer than 10 cells were removed from the dataset. Microglia clusters were digitally isolated and further filtered for clusters containing doublets, stress genes, and apoptotic cells. After filtering, the dataset from $Syk^{fl/fl}$, $Syk^{i\Delta MG}$, $Syk^{fl/fl}$-*5×FAD* and $Syk^{i\Delta MG}$-*5×FAD* mice (n = 3 for each genotype) showed in Figure 4 and S5 (refer to as SYK ONLY) contained a total of 57,830 microglia cells with a median 5871 UMI and median 2537 genes and the integration dataset from $Syk^{fl/fl}$-, $Syk^{i\Delta MG}$-, $Trem2^{+/+}$- (n = 2) and $Trem2^{-/-}$-*5×FAD* mice (n = 3) showed in Figure 5 (refer to as SYK-TREM2) contained a total of 38,404 microglia cells remained with a median 5483 UMI and median 2359 genes per cell. For *5×FAD* (n = 3), $DAP12^{K\Delta Y75}$-*5×FAD* (n = 4) dataset, cells with mitochondrial content of more than 10% were removed. Cutoffs of UMI greater than 500 and less than 100,000, and genes greater than 500 and less than 10,000 were applied. Genes expressed in fewer than 10 cells were removed from the dataset. After quality control, 26,921 microglia cells with a median 6,369 UMI and median 2,663 genes were analyzed (refer to as DAP12 ONLY). Then microglia from the DAP12 ONLY dataset were reference mapped to the UMAP of integration SYK-TREM2 dataset using FindTransferAnchors () and MapQuery () functions in the Seurat package and the UMAP was shown in Figure 6A.

Clustering and differential expression analysis—For both SYK ONLY and SYK-TREM2 datasets, data were normalized using the SCTransform method regressed on mitochondrial gene percentage and integrated using *FindIntegrationAnchors* function and Canonical Correlation Analysis (CCA) (Hafemeister and Satija, 2019; Stuart et al., 2019). Principle component analysis was performed, and the top 30 principal components were selected for dimensionality reduction using the Uniform Approximation and Projection (UMAP) algorithm. Clustering was performed using the *FindNeighbors* and *FindClusters* functions using a resolution of 0.6 (SYK ONLY) or 0.4 (SYK-TREM2). Marker genes were identified by comparing each cluster against all other clusters using the *FindAllMarkers* function with default settings (log-fold change threshold of 0.25 and >10% cells expressing the gene). Cell clusters from each tissue were annotated based on marker gene expression. For data visualization and figure preparation, the scRNA-seq data was also analyzed with BBrowser version 2.7.5 (SingleCell). Differential gene expression testing was performed using the mixed model method “dream” from the muscat package (Crowell et al., 2020). Genes detected in fewer than 10 cells or with total count less than 10 were excluded from analysis. Gene set enrichment analysis was performed with GSEA (Daly et al., 2003; Subramanian et al., 2005). Fold changes were calculated by comparing $Syk^{i\Delta MG}$-*5×FAD* vs. $Syk^{fl/fl}$-*5×FAD* on cells aggregated from TM1, TM2, and DAM clusters using *FindMarkers* with the MAST method and a nominal FDR threshold ($q < 0.05$). Genes were then ranked by log2 fold change and submitted for gene set enrichment analysis using GSEAPreranked and the hallmark gene sets from MSigDB.

Pseudotime trajectory analysis—Single-cell pseudotime trajectories were inferred using the R package *slingshot* (v2.1.0) (Street et al., 2018). Normalized values resulting from batch integration were used as input for the calculation of cell lineages and pseudotime. Genes that were significantly differentially expressed along pseudotime were identified using the R package *tradeSeq* (v1.6) (Van den Berge et al., 2020). A negative binomial generalized additive model was fit to the identified lineages using the *fitGAM* function using the top 3000 variable features. Genes that changed significantly along the DAM trajectory were identified using *associationTest*. Microglia from $Syk^{i\Delta MG}$-5×*FAD* were then compared against $Trem2^{-/-}$-5×*FAD* microglia along the DAM trajectory using the *conditionTest* function. DE genes (FDR < 0.05) were further filtered by selecting those which overlapped with those that changed significantly along the DAM trajectory.

Supplementary Material

Refer to Web version on PubMed Central for supplementary material.

ACKNOWLEDGMENTS

This work was supported by the National Institutes of Health (RF1AG05148501, R21 AG059176, and RF1 AG059082) and Centene. We thank Richard Cho for generous gift of antibodies.

DECLARATION OF INTERESTS

M. Co. is a member of Vigil Neuro scientific advisory board (SAB), is consultant for Cell Signaling Technology and NGM Bio, has received research grants from Vigil Neuro during the conduct of the study and has a patent to TREM2 pending. DMH co-founded and is on the SAB of C2N Diagnostics, is on the SAB of Denali, Genentech, and Cajal Neuroscience, consults for Alector and is on the Advisory Board for Cell. No other disclosures were reported.

REFERENCES

Askew K, Li K, Olmos-Alonso A, Garcia-Moreno F, Liang Y, Richardson P, Tipton T, Chapman MA, Riecken K, Beccari S, et al. (2017). Coupled Proliferation and Apoptosis Maintain the Rapid Turnover of Microglia in the Adult Brain. Cell Rep. 18, 391–405. [PubMed: 28076784]

Atagi Y, Liu CC, Painter MM, Chen XF, Verbeeck C, Zheng H, Li X, Rademakers R, Kang SS, Xu H, et al. (2015). Apolipoprotein E is a ligand for triggering receptor expressed on myeloid cells 2 (TREM2). J. Biol. Chem 290, 26043–26050. [PubMed: 26374899]

Van den Berge K, Roux de Bézieux H, Street K, Saelens W, Cannoodt R, Saeys Y, Dudoit S, and Clement L (2020). Trajectory-based differential expression analysis for single-cell sequencing data. Nat. Commun 11, 1201. [PubMed: 32139671]

Brown GD, Taylor PR, Reid DM, Willment JA, Williams DL, Martinez-Pomares L, Wong SYC, and Gordon S (2002). Dectin-1 is a major β-glucan receptor on macrophages. J. Exp. Med 196, 407–412. [PubMed: 12163569]

Chen Y, and Colonna M (2021). Microglia in Alzheimer's disease at single-cell level. Are there common patterns in humans and mice? J. Exp. Med 218, 1–10.

Chu DH, Morita CT, and Weiss A (1998). The Syk family of protein tyrosine kinases in T-cell activation and development. Immunol. Rev 165, 167–180. [PubMed: 9850860]

Claes C, Danhash EP, Hasselmann J, Chadarevian JP, Shabestari SK, England WE, Lim TE, Hidalgo JLS, Spitale RC, Davtyan H, et al. (2021). Plaque-associated human microglia accumulate lipid droplets in a chimeric model of Alzheimer's disease. Mol. Neurodegener 16, 50. [PubMed: 34301296]

Condello C, Yuan P, Schain A, and Grutzendler J (2015). Microglia constitute a barrier that prevents neurotoxic protofibrillar Aβ42 hotspots around plaques. Nat. Commun 6, 1–14.

Crowell HL, Soneson C, Germain PL, Calini D, Collin L, Raposo C, Malhotra D, and Robinson MD (2020). Muscat Detects Subpopulation-Specific State Transitions From Multi-Sample Multi-Condition Single-Cell Transcriptomics Data. Nat. Commun 11, 1–12. [PubMed: 31911652]

Daly MJ, Patterson N, Mesirov JP, Golub TR, Tamayo P, and Spiegelman B (2003). PGC-1α-responsive genes involved in oxidative phosphorylation are coordinately downregulated in human diabetes. Nat. Genet 34, 267–273. [PubMed: 12808457]

Eldar-Finkelman H (2002). Glycogen synthase kinase 3: An emerging therapeutic target. Trends Mol. Med 8, 126–132. [PubMed: 11879773]

Ellwanger DC, Wang S, Brioschi S, Shao Z, Green L, Case R, Yoo D, Weishuhn D, Rathanaswami P, Bradley J, et al. (2021). Prior activation state shapes the microglia response to antihuman TREM2 in a mouse model of Alzheimer's disease. Proc. Natl. Acad. Sci. U. S. A 118.

Friedman BA, Srinivasan K, Ayalon G, Meilandt WJ, Lin H, Huntley MA, Cao Y, Lee SH, Haddick PCG, Ngu H, et al. (2018). Diverse Brain Myeloid Expression Profiles Reveal Distinct Microglial Activation States and Aspects of Alzheimer's Disease Not Evident in Mouse Models. Cell Rep. 22, 832–847. [PubMed: 29346778]

Gilfillan S, Ho EL, Cella M, Yokohama WM, and Colonna M (2002). NKG2D recriuts two distinct adapters to trigger NK cell activation and costimulation. Nat. Immunol 3, 1150–1155. [PubMed: 12426564]

Ginhoux F, Greter M, Leboeuf M, Nandi S, See P, Gokhan S, Mehler MF, Conway SJ, Ng LG, Stanley ER, et al. (2010). Fate mapping analysis reveals that adult microglia derive from primitive macrophages. Science (80-.). 330, 841–845.

Goldmann T, Wieghofer P, Muller PF, Wolf Y, Varol D, Yona S, Brendecke SM, Kierdorf K, Staszewski O, Datta M, et al. (2013). A new type of microglia gene targeting shows TAK1 to be pivotal in CNS autoimmune inflammation. Nat. Neurosci 16, 1618–1626. [PubMed: 24077561]

Goldmann T, Wieghofer P, Jordão MJC, Prutek F, Hagemeyer N, Frenzel K, Amann L, Staszewski O, Kierdorf K, Krueger M, et al. (2016). Origin, fate and dynamics of macrophages at central nervous system interfaces. Nat. Immunol 17, 797–805. [PubMed: 27135602]

Gomez Perdiguero E, Klapproth K, Schulz C, Busch K, Azzoni E, Crozet L, Garner H, Trouillet C, De Bruijn MF, Geissmann F, et al. (2015). Tissue-resident macrophages originate from yolk-sac-derived erythro-myeloid progenitors. Nature 518, 547–551. [PubMed: 25470051]

Hafemeister C, and Satija R (2019). Normalization and variance stabilization of single-cell RNA-seq data using regularized negative binomial regression. BioRxiv 576827.

Hamerman JA, Ni M, Killebrew JR, Chu CL, and Lowell CA (2009). The expanding roles of ITAM adapters FcRγ and DAP12 in myeloid cells. Immunol. Rev 232, 42–58. [PubMed: 19909355]

Hao Y, Hao S, Andersen-Nissen E, Mauck WM, Zheng S, Butler A, Lee MJ, Wilk AJ, Darby C, Zager M, et al. (2021). Integrated analysis of multimodal single-cell data. Cell 184, 3573–3587.e29. [PubMed: 34062119]

Herre J, Marshall ASJ, Caron E, Edwards AD, Williams DL, Schweighoffer E, Tybulewicz V, Reis E Sousa C, Gordon S, and Brown GD (2004). Dectin-1 uses novel mechanisms for yeast phagocytosis in macrophages. Blood 104, 4038–4045. [PubMed: 15304394]

Jay TR, Miller CM, Cheng PJ, Graham LC, Bemiller S, Broihier ML, Xu G, Margevicius D, Karlo JC, Sousa GL, et al. (2015). TREM2 deficiency eliminates TREM2^{+} inflammatory macrophages and ameliorates pathology in Alzheimer's disease mouse models. J. Exp. Med 212, 287–295. [PubMed: 25732305]

Jay TR, Hirsch AM, Broihier ML, Miller CM, Neilson LE, Ransohoff RM, Lamb BT, and Landreth GE (2017). Disease progression-dependent effects of TREM2 deficiency in a mouse model of Alzheimer's disease. J. Neurosci 37, 637–647. [PubMed: 28100745]

Keren-Shaul H, Spinrad A, Weiner A, Matcovitch-Natan O, Dvir-Szternfeld R, Ulland TK, David E, Baruch K, Lara-Astaiso D, Toth B, et al. (2017). A Unique Microglia Type Associated with Restricting Development of Alzheimer's Disease. Cell 169, 1276–1290.e17. [PubMed: 28602351]

Krasemann S, Madore C, Cialic R, Baufeld C, Calcagno N, El Fatimy R, Beckers L, O'Loughlin E, Xu Y, Fanek Z, et al. (2017). The TREM2-APOE Pathway Drives the Transcriptional Phenotype of Dysfunctional Microglia in Neurodegenerative Diseases. Immunity 47, 566–581.e9. [PubMed: 28930663]

Lanier LL (2009). DAP10- and DAP12-associated receptors in innate immunity. Immunol. Rev 227, 150–160. [PubMed: 19120482]

Lee SH, Meilandt WJ, Xie L, Gandham VD, Ngu H, Barck KH, Rezzonico MG, Imperio J, Lalehzadeh G, Huntley MA, et al. (2021). Trem2 restrains the enhancement of tau accumulation and neurodegeneration by β-amyloid pathology. Neuron 109, 1283–1301.e6. [PubMed: 33675684]

Long JM, and Holtzman DM (2019). Alzheimer Disease: An Update on Pathobiology and Treatment Strategies. Cell 1–28.

Marsh SE, Walker AJ, Kamath T, Dissing-Olesen L, Hammond TR, de Soysa TY, Young AMH, Murphy S, Abdulraouf A, Nadaf N, et al. (2022). Dissection of artifactual and confounding glial signatures by single-cell sequencing of mouse and human brain. Nat. Neurosci 25, 306–316. [PubMed: 35260865]

Mass E, Jacome-Galarza CE, Blank T, Lazarov T, Durham BH, Ozkaya N, Pastore A, Schwabenland M, Chung YR, Rosenblum MK, et al. (2017). A somatic mutation in erythro-myeloid progenitors causes neurodegenerative disease. Nature 549, 389–393. [PubMed: 28854169]

Masters CL, and Selkoe DJ (2012). Biochemistry of amyloid β-protein and amyloid deposits in Alzheimer disease. Cold Spring Harb. Perspect. Med 2.

Masuda T, Amann L, Monaco G, Sankowski R, Staszewski O, Krueger M, Del Gaudio F, He L, Paterson N, Nent E, et al. (2022). Specification of CNS macrophage subsets occurs postnatally in defined niches. Nature 604, 740–748. [PubMed: 35444273]

Mathys H, Adaikkan C, Gao F, Young JZ, Manet E, Hemberg M, De Jager PL, Ransohoff RM, Regev A, and Tsai LH (2017). Temporal Tracking of Microglia Activation in Neurodegeneration at Single-Cell Resolution. Cell Rep. 21, 366–380. [PubMed: 29020624]

Mócsai A, Abram CL, Jakus Z, Hu Y, Lanier LL, and Lowell CA (2006). Integrin signaling in neutrophils and macrophages uses adaptors containing immunoreceptor tyrosine-based activation motifs. Nat. Immunol 7, 1326–1333. [PubMed: 17086186]

Molgora M, Esaulova E, Vermi W, Hou J, Chen Y, Luo J, Brioschi S, Bugatti M, Omodei AS, Ricci B, et al. (2020). TREM2 Modulation Remodels the Tumor Myeloid Landscape Enhancing Anti-PD-1 Immunotherapy. Cell 182, 886–900.e17. [PubMed: 32783918]

Mucke L, and Selkoe DJ (2012). Neurotoxicity of amyloid β-protein: Synaptic and network dysfunction. Cold Spring Harb. Perspect. Med 2, 1–18.

Nugent AA, Lin K, van Lengerich B, Lianoglou S, Przybyla L, Davis SS, Llapashtica C, Wang J, Kim DJ, Xia D, et al. (2020). TREM2 Regulates Microglial Cholesterol Metabolism upon Chronic Phagocytic Challenge. Neuron 105, 837–854.e9. [PubMed: 31902528]

Oakley H, Cole SL, Logan S, Maus E, Shao P, Craft J, Guillozet-Bongaarts A, Ohno M, Disterhoft J, Van Eldik L, et al. (2006). Intraneuronal β-amyloid aggregates, neurodegeneration, and neuron loss in transgenic mice with five familial Alzheimer's disease mutations: Potential factors in amyloid plaque formation. J. Neurosci 26, 10129–10140. [PubMed: 17021169]

Peng Q, Malhotra S, Torchia JA, Kerr WG, Coggeshall KM, and Humphrey MB (2010). TREM2- and DAP12-dependent activation of PI3K requires DAP10 and is inhibited by SHIP1. Sci. Signal 3, 1–16.

Prinz M, Masuda T, Wheeler MA, and Quintana FJ (2021). Microglia and Central Nervous System-Associated Macrophages mdash from Origin to Disease Modulation. Annu. Rev. Immunol 39, 251–277. [PubMed: 33556248]

Rogers NC, Slack EC, Edwards AD, Nolte MA, Schulz O, Schweighoffer E, Williams DL, Gordon S, Tybulewicz VL, Brown GD, et al. (2005). Syk-dependent cytokine induction by dectin-1 reveals a novel pattern recognition pathway for C type lectins. Immunity 22, 507–517. [PubMed: 15845454]

Safaiyan S, Besson-Girard S, Kaya T, Cantuti-Castelvetri L, Liu L, Ji H, Schifferer M, Gouna G, Usifo F, Kannaiyan N, et al. (2021). White matter aging drives microglial diversity. Neuron 109, 1100–1117.e10. [PubMed: 33606969]

Saijo K, Schmedt C, Su I hsin, Karasuyama H, Lowell CA, Reth M, Adachi T, Patke A, Santana A, and Tarakhovsky A (2003). Essential role of Src-family protein tyrosine kinases in NF-κB activation during B cell development. Nat. Immunol 4, 274–279. [PubMed: 12563261]

Sala Frigerio C, Wolfs L, Fattorelli N, Thrupp N, Voytyuk I, Schmidt I, Mancuso R, Chen WT, Woodbury ME, Srivastava G, et al. (2019). The Major Risk Factors for Alzheimer's Disease: Age,

Sex, and Genes Modulate the Microglia Response to Aβ Plaques. Cell Rep. 27, 1293–1306.e6. [PubMed: 31018141]

Schulz C, Perdiguero EG, Chorro L, Szabo-Rogers H, Cagnard N, Kierdorf K, Prinz M, Wu B, Jacobsen SEW, Pollard JW, et al. (2012). A lineage of myeloid cells independent of myb and hematopoietic stem cells. Science (80-.). 335, 86–90.

Song WM, Joshita S, Zhou Y, Ulland TK, Gilfillan S, and Colonna M (2018). Humanized TREM2 mice reveal microglia-intrinsic and -extrinsic effects of R47H polymorphism. J. Exp. Med 215, 745–760. [PubMed: 29321225]

Spangenberg E, Severson PL, Hohsfield LA, Crapser J, Zhang J, Burton EA, Zhang Y, Spevak W, Lin J, Phan NY, et al. (2019). Sustained microglial depletion with CSF1R inhibitor impairs parenchymal plaque development in an Alzheimer's disease model. Nat. Commun 10, 1–21. [PubMed: 30602773]

Street K, Risso D, Fletcher RB, Das D, Ngai J, Yosef N, Purdom E, and Dudoit S (2018). Slingshot: cell lineage and pseudotime inference for single-cell transcriptomics. BMC Genomics 19, 477. [PubMed: 29914354]

Stuart T, Butler A, Hoffman P, Hafemeister C, Papalexi E, Mauck WM, Hao Y, Stoeckius M, Smibert P, and Satija R (2019). Comprehensive Integration of Single-Cell Data. Cell 177, 1888–1902.e21. [PubMed: 31178118]

Subramanian A, Tamayo P, Mootha VK, Mukherjee S, Ebert BL, Gillette MA, Paulovich A, Pomeroy SL, Golub TR, Lander ES, et al. (2005). Gene set enrichment analysis: a knowledge-based approach for interpreting genome-wide expression profiles. Proc. Natl. Acad. Sci. U. S. A 102, 15545–15550. [PubMed: 16199517]

Tay TL, Mai D, Dautzenberg J, Fernández-Klett F, Lin G, Sagar S, Datta M, Drougard A, Stempfl T, Ardura-Fabregat A, et al. (2017). A new fate mapping system reveals context-dependent random or clonal expansion of microglia. Nat. Neurosci 20, 793–803. [PubMed: 28414331]

Thion MS, Ginhoux F, and Garel S (2018). Microglia and early brain development: An intimate journey. Science (80-.). 362, 185–189.

Tomasello E, Desmoulins PO, Chemin K, Guia S, Cremer H, Ortaldo J, Love P, Kaiserlian D, and Vivier E (2000). Combined natural killer cell and dendritic cell functional deficiency in KARAP/DAP12 loss-of-function mutant mice. Immunity 13, 355–364. [PubMed: 11021533]

Turner M, Schweighoffer E, Colucci F, Di Santo JP, and Tybulewicz VL (2000). Tyrosine kinase SYK: Essential functions for immunoreceptor signalling. Immunol. Today 21, 148–154. [PubMed: 10689303]

Ulland TK, and Colonna M (2018). TREM2 — a key player in microglial biology and Alzheimer disease. Nat. Rev. Neurol 14, 667–675. [PubMed: 30266932]

Ulland TK, Song WM, Huang SCC, Ulrich JD, Sergushichev A, Beatty WL, Loboda AA, Zhou Y, Cairns NJ, Kambal A, et al. (2017). TREM2 Maintains Microglial Metabolic Fitness in Alzheimer's Disease. Cell 170, 649–663.e13. [PubMed: 28802038]

Underhill DM, Rossnagle E, Lowell CA, and Simmons RM (2005). Dectin-1 activates Syk tyrosine kinase in a dynamic subset of macrophages for reactive oxygen production. Blood 106, 2543–2550. [PubMed: 15956283]

Utz SG, See P, Mildenberger W, Thion MS, Silvin A, Lutz M, Ingelfinger F, Rayan NA, Lelios I, Buttgereit A, et al. (2020). Early Fate Defines Microglia and Non-parenchymal Brain Macrophage Development. Cell 181, 557–573.e18. [PubMed: 32259484]

Wang S, Mustafa M, Yuede CM, Salazar SV, Kong P, Long H, Ward M, Siddiqui O, Paul R, Gilfillan S, et al. (2020). Anti-human TREM2 induces microglia proliferation and reduces pathology in an Alzheimer's disease model. J. Exp. Med 217.

Wang Y, Cella M, Mallinson K, Ulrich JD, Young KL, Robinette ML, Gilfillan S, Krishnan GM, Sudhakar S, Zinselmeyer BH, et al. (2015). TREM2 lipid sensing sustains the microglial response in an Alzheimer's disease model. Cell 160, 1061–1071. [PubMed: 25728668]

Wang Y, Ulland TK, Ulrich JD, Song W, Tzaferis JA, Hole JT, Yuan P, Mahan TE, Shi Y, Gilfillan S, et al. (2016). TREM2-mediated early microglial response limits diffusion and toxicity of amyloid plaques. J. Exp. Med 213, 667–675. [PubMed: 27091843]

Wes PD, Sayed FA, Bard F, and Gan L (2016). Targeting microglia for the treatment of Alzheimer's Disease. Glia 64, 1710–1732. [PubMed: 27100611]

Wozniak DF, Hartman RE, Boyle MP, Vogt SK, Brooks AR, Tenkova T, Young C, Olney JW, and Muglia LJ (2004). Apoptotic neurodegeneration induced by ethanol in neonatal mice is associated with profound learning/memory deficits in juveniles followed by progressive functional recovery in adults. Neurobiol. Dis 17, 403–414. [PubMed: 15571976]

Wozniak DF, Diggs-Andrews KA, Conyers S, Yuede CM, Dearborn JT, Brown JA, Tokuda K, Izumi Y, Zorumski CF, and Gutmann DH (2013). Motivational Disturbances and Effects of L-dopa Administration in Neurofibromatosis-1 Model Mice. PLoS One 8.

Wright GJ, Cherwinski H, Foster-Cuevas M, Brooke G, Puklavec MJ, Bigler M, Song Y, Jenmalm M, Gorman D, McClanahan T, et al. (2003). Characterization of the CD200 Receptor Family in Mice and Humans and Their Interactions with CD200. J. Immunol 171, 3034–3046. [PubMed: 12960329]

Xiong M, Jiang H, Serrano JR, Gonzales ER, Wang C, Gratuze M, Hoyle R, Bien-Ly N, Silverman AP, Sullivan PM, et al. (2021). APOE immunotherapy reduces cerebral amyloid angiopathy and amyloid plaques while improving cerebrovascular function. Sci. Transl. Med 13, 1–13.

Yamanishi Y, Kitaura J, Izawa K, Matsuoka T, Oki T, Lu Y, Shibata F, Yamazaki S, Kumagai H, Nakajima H, et al. (2008). Analysis of mouse LMIR5/CLM-7 as an activating receptor: Differential regulation of LMIR5/CLM-7 in mouse versus human cells. Blood 111, 688–698. [PubMed: 17928527]

Yao H, Coppola K, Schweig JE, Crawford F, Mullan M, and Paris D (2019). Distinct Signaling Pathways Regulate TREM2 Phagocytic and NFκB Antagonistic Activities. Front. Cell. Neurosci 13, 1–18. [PubMed: 30723396]

Yeh FL, Wang Y, Tom I, Gonzalez LC, and Sheng M (2016). TREM2 Binds to Apolipoproteins, Including APOE and CLU/APOJ, and Thereby Facilitates Uptake of Amyloid-Beta by Microglia. Neuron 91, 328–340. [PubMed: 27477018]

Yona S, Kim KW, Wolf Y, Mildner A, Varol D, Breker M, Strauss-Ayali D, Viukov S, Guilliams M, Misharin A, et al. (2013). Fate Mapping Reveals Origins and Dynamics of Monocytes and Tissue Macrophages under Homeostasis. Immunity 38, 79–91. [PubMed: 23273845]

Yuan P, Condello C, Keene CD, Wang Y, Bird TD, Paul SM, Luo W, Colonna M, Baddeley D, and Grutzendler J (2016). TREM2 Haplodeficiency in Mice and Humans Impairs the Microglia Barrier Function Leading to Decreased Amyloid Compaction and Severe Axonal Dystrophy. Neuron 90, 724–739. [PubMed: 27196974]

Zhao Y, Wu X, Li X, Jiang LL, Gui X, Liu Y, Sun Y, Zhu B, Piña-Crespo JC, Zhang M, et al. (2018). TREM2 Is a Receptor for β-Amyloid that Mediates Microglial Function. Neuron 97, 1023–1031.e7. [PubMed: 29518356]

Zhou Y, Song WM, Andhey PS, Swain A, Levy T, Miller KR, Poliani PL, Cominelli M, Grover S, Gilfillan S, et al. (2020). Human and mouse single-nucleus transcriptomics reveal TREM2-dependent and TREM2-independent cellular responses in Alzheimer's disease. Nat. Med 26, 131–142. [PubMed: 31932797]

Ziegenfuss JS, Biswas R, Avery MA, Hong K, Sheehan AE, Yeung Y-G, Stanley ER, and Freeman MR (2008). Draper-dependent glial phagocytic activity is mediated by Src and Syk family kinase signalling. Nature 453, 935–939. [PubMed: 18432193]

(2021). 2021 Alzheimer's disease facts and figures. Alzheimers. Dement 17, 327–406. [PubMed: 33756057]

- Microglia must activate SYK to restrain Aβ pathology
- SYK sustains microglia fitness through the PI3K-AKT-GSK3β-mTOR pathway
- TREM2 activates microglia through SYK and SYK-independent DAP10-dependent pathways
- Direct activation of SYK by anti-CLEC7A rescues microglia with hypofunctional TREM2

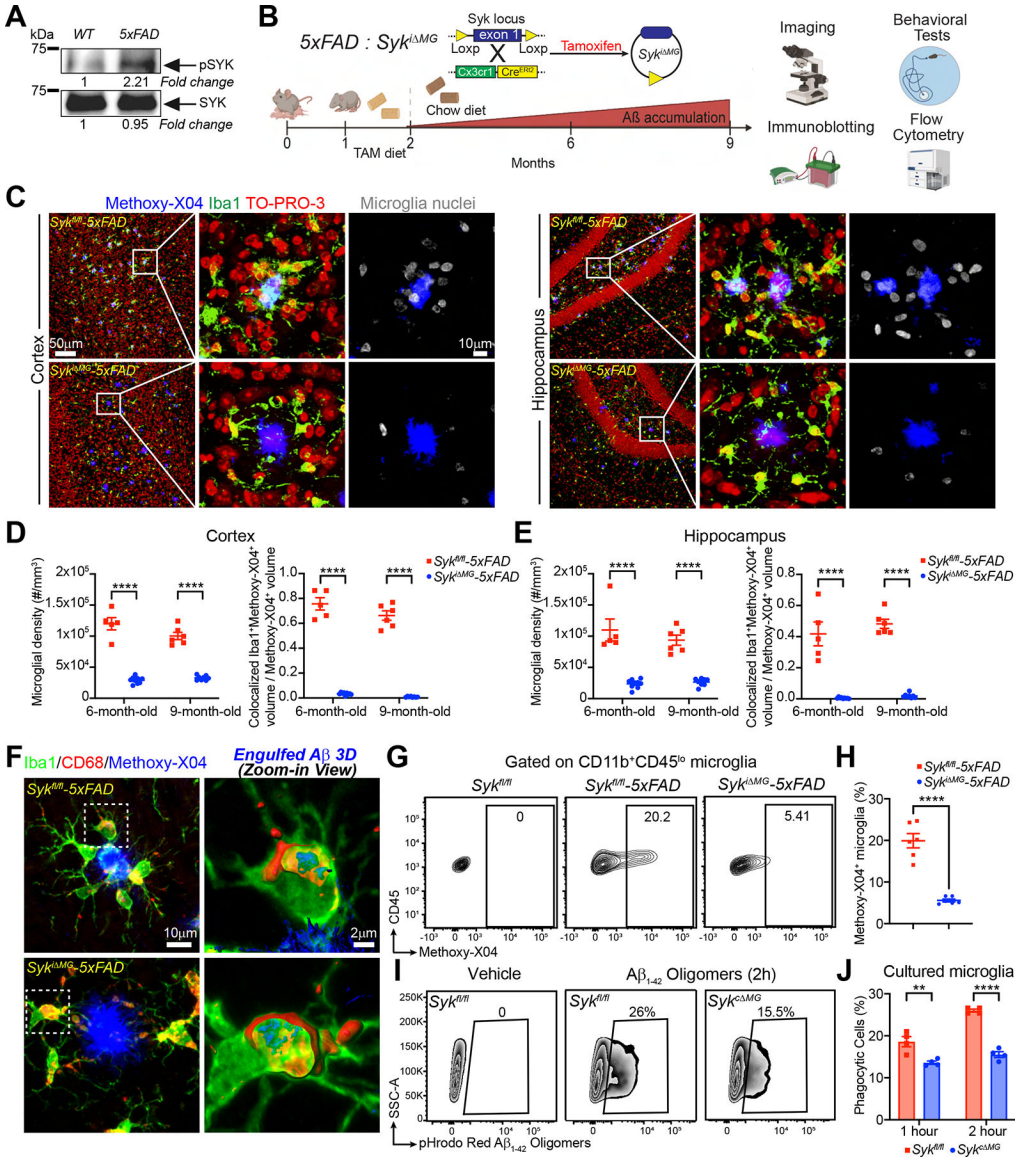

Figure 1. Conditional deletion of *Syk* in microglia abolishes their capacity to respond to Aβ plaques and uptake Aβ

(A) Immunoblot of SYK and pSYK protein on sorted microglia from 8-month-old WT and *5×FAD* mice. Representative of two independent experiments.

(B) Schematic of the experimental design.

(C) Representative confocal images of cortex and dentate gyrus from 9-month-old $Syk^{fl/fl}$- and $Syk^{i\Delta MG}$-*5×FAD* mice.

(D and E) Quantification of microglia density within a 15-µm radius from the plaque surfaces and Iba1^{+}methoxy-X04^{+} colocalization volume normalized by total methoxy-X04^{+} volume, in either cortex or hippocampus of 6- and 9- month-old mice of each genotype. Data points represent the average of two technical repeats (one experiment; n = 5–9 mice/genotype).

(F) 3D reconstruction of microglia from 6-month-old $Syk^{fl/fl}$- and $Syk^{i\Delta MG}$-*5×FAD* mice, showing engulfed Aβ inside CD68^{+} phagosomes.

(G) Representative FACS plots of methoxy-X04^{+} microglia from 6-month-old *Syk*$^{fl/fl}$, *Syk*$^{fl/fl}$-*5×FAD* and *Syk*$^{i\Delta MG}$-*5×FAD* mice.
(H) Percentage of methoxy-X04^{+} microglia from each genotype (two independent experiments; n = 6 mice/genotype).
(I) Representative FACS plots of *Syk*$^{fl/fl}$ and *Syk*$^{c\Delta MG}$ primary microglia cultured with pHrodo-Red labeled A$\beta_{1–42}$ for 2 hours.
(J) Quantification of A$\beta_{1–42}$ uptake by primary microglia from each genotype. Representative of three independent experiments (n = 4 technical repeats/group).
**, P < 0.01; ****, P < 0.0001- by two-way ANOVA with Sidak's multiple comparisons test (D, E and J), or two-tailed unpaired Student's t test (H). Data are presented as mean ± SEM. See also Figure S1 in the supplemental information.

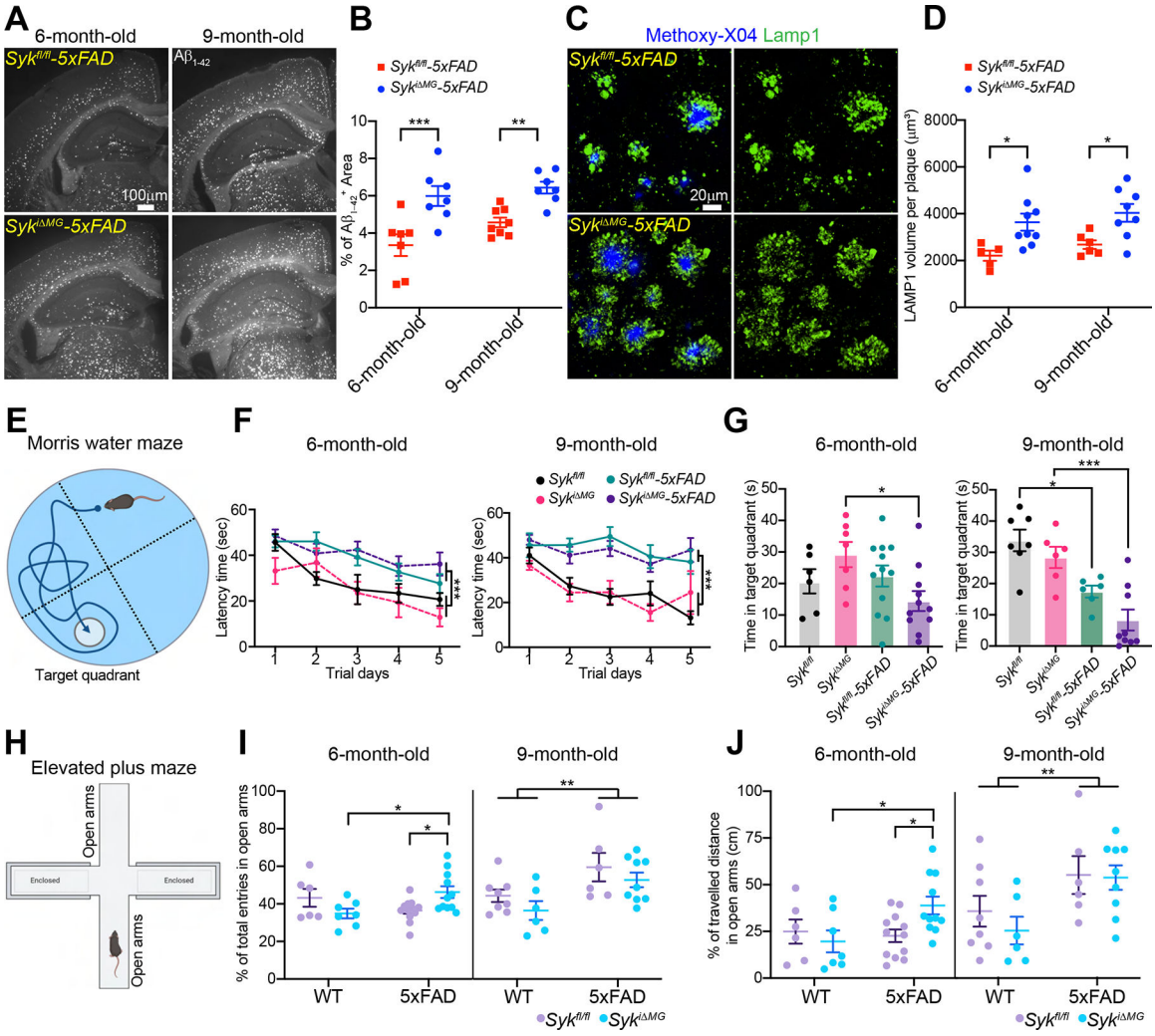

Figure 2. SYK deficiency in microglia exacerbates Aβ pathology and leads to behavior and memory defects

(A) Representative images of $A\beta_{1–42}$ staining in 6- and 9-month-old *Syk$^{fl/fl}$-5×FAD* and *Syk^{iΔMG}-5×FAD* mice.

(B) Percentage of $A\beta_{1–42}^{+}$ area in the cortex of 6- and 9-month-old mice of each genotype. Data points represent the average of three technical repeats (one experiment; n = 7–8 mice/genotype).

(C) Representative confocal images of methoxy-X04 and $Lamp1^{+}$ dystrophic neurites in the cortex of 9-month-old *Syk$^{fl/fl}$-5×FAD* and *Syk^{iΔMG}-5×FAD* mice.

(D) Volumes of dystrophic neurites per plaque in 6- and 9-month-old mice of each genotype. Data points represent the average of two technical repeats (one experiment; n = 5–9 mice/genotype).

(E-G) Morris water maze tests on 6- and 9-month-old *Syk$^{fl/fl}$* and *Syk^{iΔMG}* mice with or without *5×FAD* transgenes. F) Latency time to submerged platform; (G) time in target quadrant without submerged platform.

(H-J) Elevated plus maze test on 6- and 9-month-old $Syk^{fl/fl}$ and $Syk^{i\Delta MG}$ mice with or without *5×FAD* transgenes. (I) Percentage of entries into open arms; (J) percentage of travelled distance in open arms.

Sample size of behavioral tests: 6-month-old $Syk^{fl/fl}$ (n=6), $Syk^{i\Delta MG}$ (n=7), $Syk^{fl/fl}$-*5×FAD* (n=12) and $Syk^{i\Delta MG}$-*5×FAD* (n=11); 9-month-old $Syk^{fl/fl}$ (n=7), $Syk^{i\Delta MG}$ (n=6), $Syk^{fl/fl}$-*5×FAD* (n=6) and $Syk^{i\Delta MG}$-*5×FAD* (n=9). *, $P < 0.05$; **, $P < 0.01$; ***, $P < 0.001$ by two-way ANOVA with Sidak's multiple comparisons test (B, D, F, I and J), or one-way ANOVA with Tukey's multiple comparisons test (G). Data are presented as mean ± SEM.

See also Figure S2 in the supplemental information.

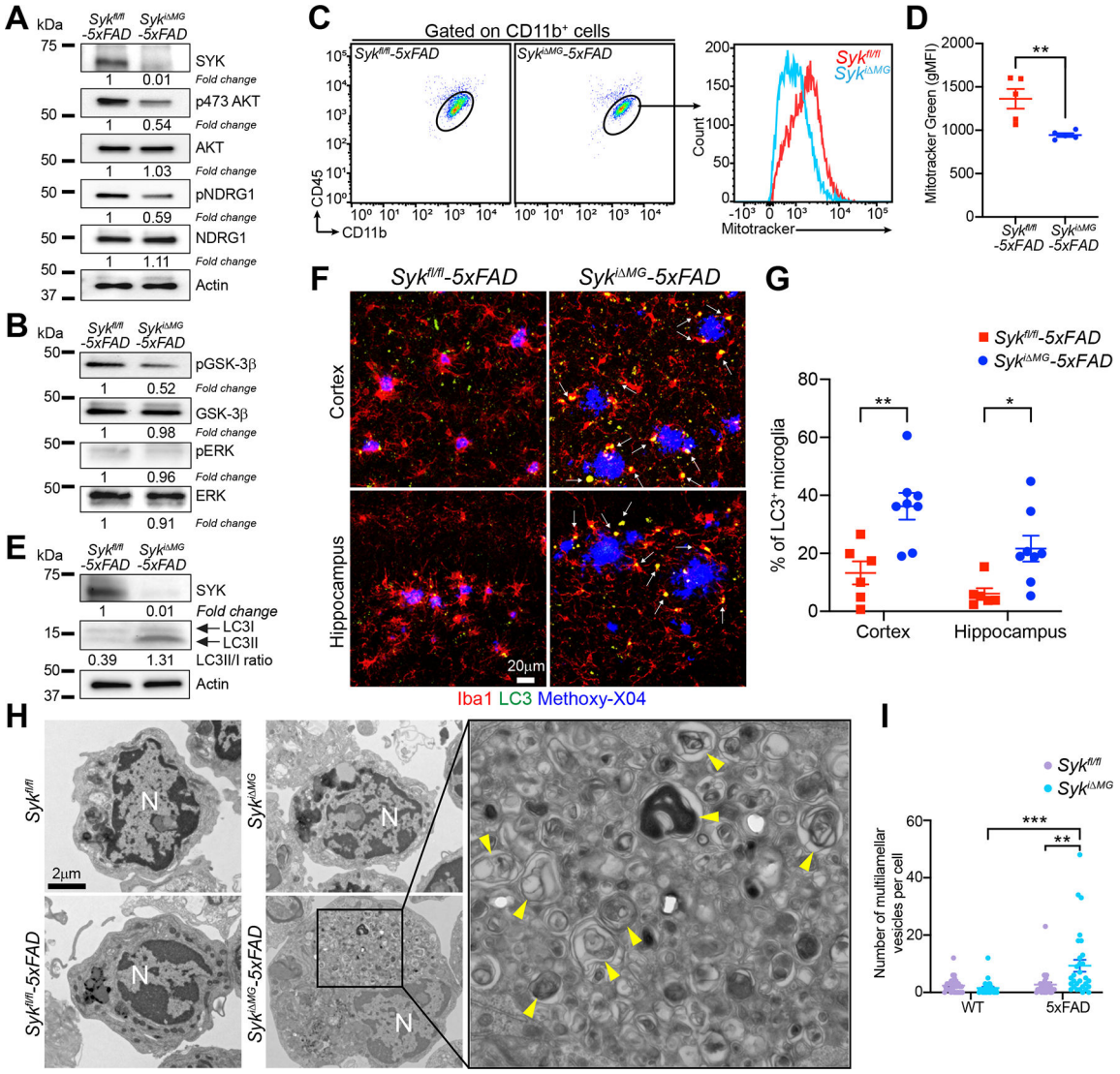

Figure 3. SYK deficiency impairs the PI3K-AKT-GSK3-β-mTOR axis, and augments autophagy in microglia of *5×FAD* mice

(A and B) Immunoblots of the indicated molecules on sorted microglia from 9-month-old *Syk$^{fl/fl}$-5×FAD* and *Syk^{iΔMG}-5×FAD* mice. Representative of two independent experiments.

(C and D) Quantification of mitochondrial mass in microglia from 9-month-old *Syk$^{fl/fl}$-5×FAD* and *Syk^{iΔMG}-5×FAD* mice assessed by MitoTracker Green incorporation (two independent experiments; n = 5 mice/genotype).

(E) Immunoblot of the LC3II/LC3I ratio on sorted microglia from 9-month-old *Syk$^{fl/fl}$-5×FAD* and *Syk^{iΔMG}-5×FAD* mice. Representative of two independent experiments.

(F) Representative confocal images of methoxy-X04, Iba1, and LC3 staining in the cortex and hippocampus of 9-month-old *Syk$^{fl/fl}$-5×FAD* and *Syk^{iΔMG}-5×FAD* mice (arrows indicate microglial LC3^{+} vesicles).

(G) Percentage of LC3^{+} microglia in 9-month-old mice of each genotype. Data points represent the average of two technical repeats (one experiment; n = 6–8 mice/genotype).

(H) Representative TEM images of microglia sorted from 9-month-old $Syk^{fl/fl}$ and $Syk^{i\Delta MG}$ mice, with or without *5×FAD* transgenes (N = nucleus; yellow arrowheads = multivesicular structures).

(I) Number of multivesicular structures per microglia (n = 30 cells/genotype).

*, P < 0.05; **, P < 0.01; ***, P < 0.001 by two-tailed unpaired Student's t test (D), or two-way ANOVA with Sidak's multiple comparisons test (G and I). Data are presented as mean ± SEM.

See also Figure S3 in the supplemental information.

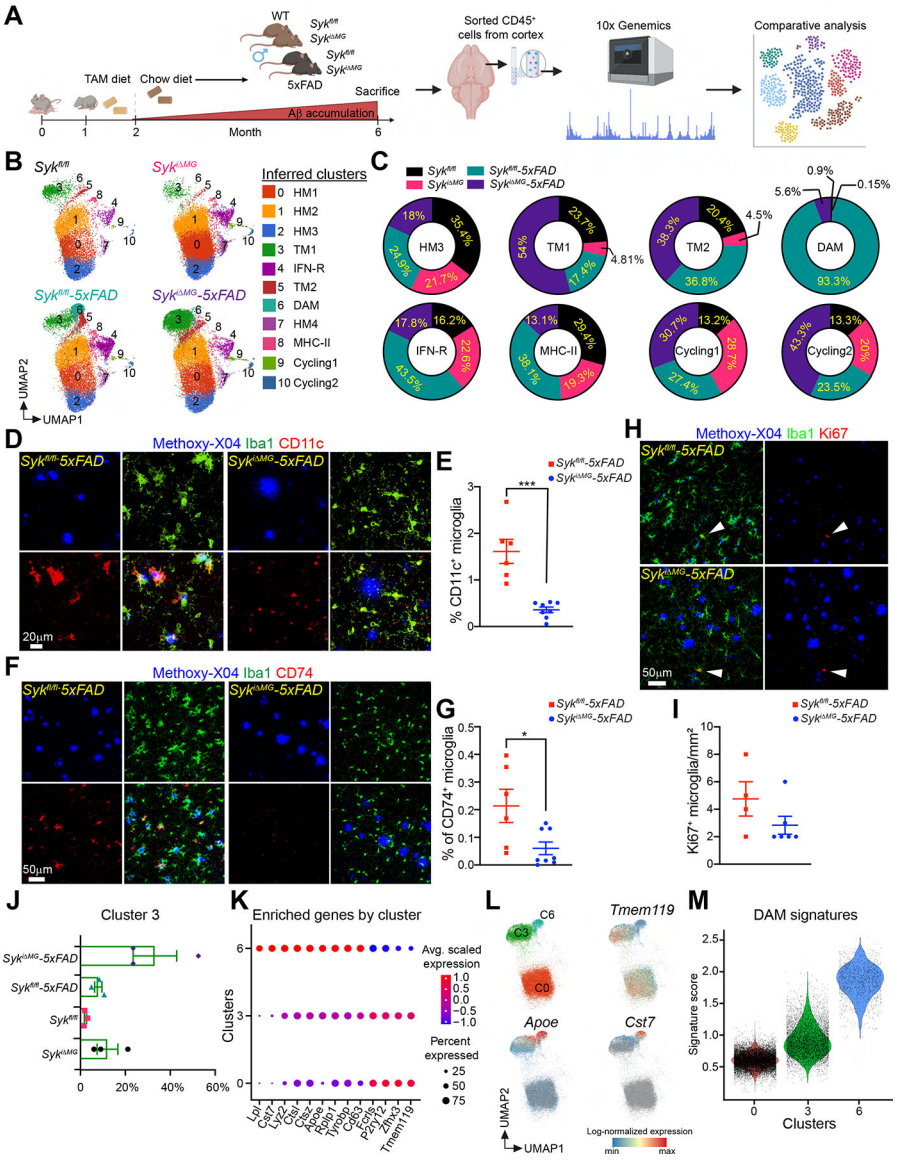

Figure 4. SYK deficiency in microglia hampers microglial activation in *5×FAD* mice

(A) Schematic of the experimental design.

(B) UMAP plots of microglia from each genotype (n = 3 mice/genotype). Cluster annotation based on expression of signature genes shown in Figure S5.

(C) Proportional contribution of each genotype to designated clusters.

(D and F) Representative confocal images of methoxy-X04, Iba-1 and CD11c or CD74 staining in the cortex of 6-month-old $Syk^{fl/fl}$-*5×FAD* and $Syk^{i\Delta MG}$-*5×FAD* mice.

(E and G) Percentage of $CD11c^{+}$ or $CD74^{+}$ microglia in the cortex of each genotype. Data points represent the average of two technical repeats (one experiment; n = 6–8 mice/genotype).

(H) Representative confocal images of methoxy-X04, Iba-1, and Ki67 in the cortex of 6-month-old $Syk^{fl/fl}$-*5×FAD* and $Syk^{i\Delta MG}$-*5×FAD* mice.

(I) Quantification of $Ki67^+$ microglia from indicated mice. Data points represent the average of two technical repeats (representative of two independent experiments; white arrows indicate $Ki67^+$ microglia; n = 4–6 mice/genotype).
(J) Relative abundance of cluster 3 (TM1) in all genotypes.
(K) Average scaled expression levels of selected signature genes for clusters 0 (HM1), 3 (TM1) and 6 (DAM).
(L) UMAP plots showing enrichment of selected signature in clusters 0 (HM1), 3 (TM1) and 6 (DAM).
(M) Violin plots of the DAM signature scores in clusters 0 (HM1), 3 (TM1) and 6 (DAM).
*, $P < 0.05$; ***, $P < 0.001$ by two-tailed unpaired Student's t test. Data are presented as mean ± SEM.
See also Figure S5 and S6 in the supplemental information.

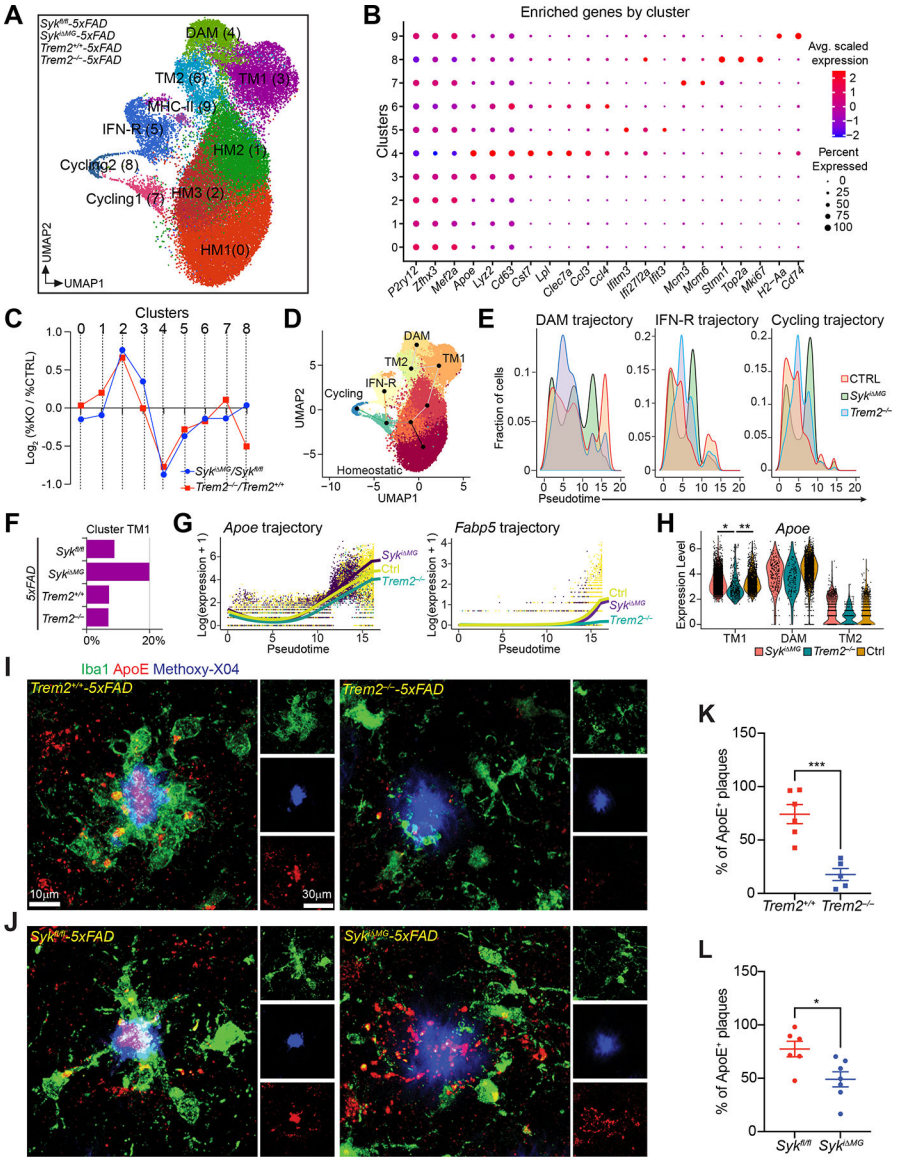

Figure 5. scRNA-seq reveals distinct defects in the DAM trajectories of SYK- and TREM2-deficient microglia

(A) UMAP plots of microglia from each genotype (n = 2–3 mice/genotype).

(B) Average scaled expression levels of selected signature genes per cluster.

(C) Log2 fold-change of cluster sizes in $Syk^{i\Delta MG}$-5×*FAD* and $Trem2^{-/-}$-5×*FAD* respective to controls ($Syk^{fl/fl}$-5×*FAD and* $Trem2^{+/+}$-5×*FAD*).

(D) UMAP plot showing the projection of the three identified phenotypic trajectories.

(E) Pseudotime distribution of microglia from each genotype along DAM, IFN-R, and cycling trajectories. CTRL group is a pool of microglia from $Syk^{fl/fl}$-5×*FAD* and $Trem2^{+/+}$-5×*FAD* mice.

(F) Relative abundance of cluster TM1 for each genotype.

(G) Expression levels of *Apoe* and *Fabp5* along the DAM trajectory for indicated genotypes. CTRL group is a pool of microglia from $Syk^{fl/fl}$-5×*FAD* and $Trem2^{+/+}$-5×*FAD* mice.

(H) Violin plots comparing *Apoe* expression among indicated genotypes in selected clusters (TM1, TM2 and DAM). CTRL group is a pool of microglia from *Syk*$^{fl/fl}$-*5×FAD* and *Trem2*$^{+/+}$-*5×FAD* mice.

(I and J) Representative confocal images of methoxy-X04, Iba-1 and ApoE staining the cortex of 6-month-old *Trem2*$^{+/+}$-*5×FAD*, *Trem2*$^{-/-}$-*5×FAD*, *Syk*$^{fl/fl}$-*5×FAD* and *Syk*$^{i\Delta MG}$-*5×FAD* mice.

(K and L) Percentage of ApoE-positive plaques in each genotype. Data points represent the average of two technical repeats (one experiment; n = 5–7 mice/genotype).

*, P < 0.05; **, P < 0.01; ***, P < 0.001 by two-tailed unpaired Student's t test (K and L), or mixed model (H) (see METHOD DETAILS). Data are presented as mean ± SEM.

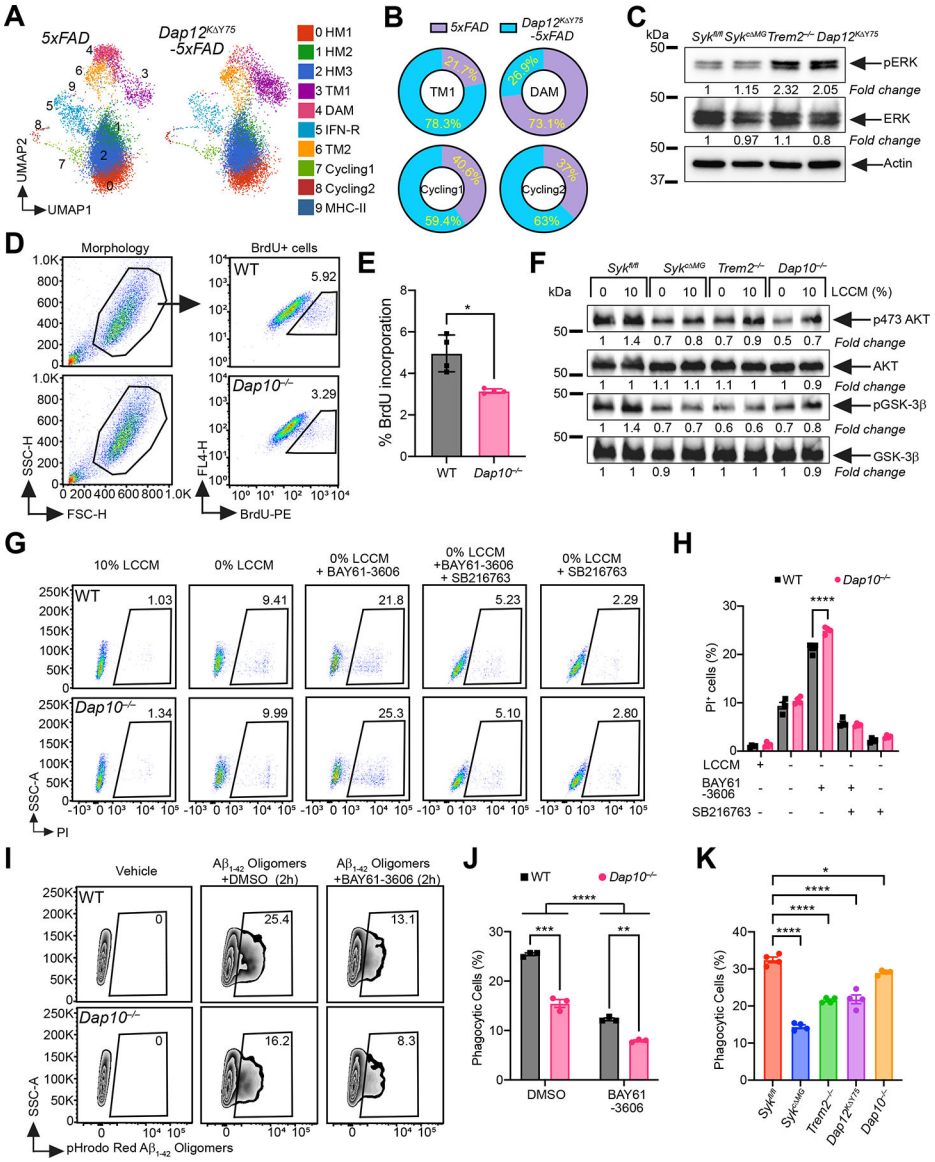

Figure 6. DAP10 activates microglia independently of SYK

(A) UMAP plots of microglia from each genotype (n = 3–4 mice/genotype). Cluster annotation based on expression of signature genes shown in Figure 5B and S5.

(B) Proportional contribution of each genotype to designated clusters.

(C) Immunoblots of ERK and pERK on BMDM from indicated genotypes. Representative of two independent experiments.

(D) Representative FACS plots of BrdU staining on WT and *Dap10*$^{-/-}$ primary microglia.

(E) Percentage of BrdU^{+} microglia in each genotype. Representative of three independent experiments (n = 4 technical repeats/genotype).

(F) Immunoblots of AKT, pSer473 AKT, GSK3-β and pGSK3-β on cultured primary microglia from indicated genotypes, with or without 10% LCCM stimulation. Representative of two independent experiments.

(G) Representative FACS plots of PI staining on WT and *Dap10*$^{-/-}$ BMDM, cultured 48 hours under five different conditions: 1) 10% LCCM; 2) 0% LCCM; 3) 0% LCCM + BAY61–3606 (SYK inhibitor); 4) 0% LCCM + BAY61–3606 + SB216763 (GSK-3β inhibitor); 5) 0% LCCM $^{+}$ SB216763.

(H) Percentage of dead BMDMs in each genotype, at the indicated conditions. Representative of three independent experiments (n = 4 technical repeats/group).

(I) Representative FACS plots of WT and *Dap10*$^{-/-}$ BMDMs cultured with pHrodo-Red labeled Aβ_{1-42} for 2 hours, with or without SYK inhibitor.

(J) Quantification of Aβ_{1-42} uptake by BMDMs from each genotype, with or without SYK inhibitor. Representative of three independent experiments (n = 3 technical repeats/group).

(K) Same experiment as in (I and J), on BMDMs of indicated genotypes. Representative of three independent experiments (n = 4 technical repeats/genotype).

*, $P < 0.05$; **, $P < 0.01$; ***, $P < 0.001$; ****, $P < 0.0001$ by two-tailed unpaired Student's t test (E), two-way ANOVA with Sidak's multiple comparisons test (H and J), or one-way ANOVA with Tukey's multiple comparisons test (K). Data are presented as mean ± SEM.

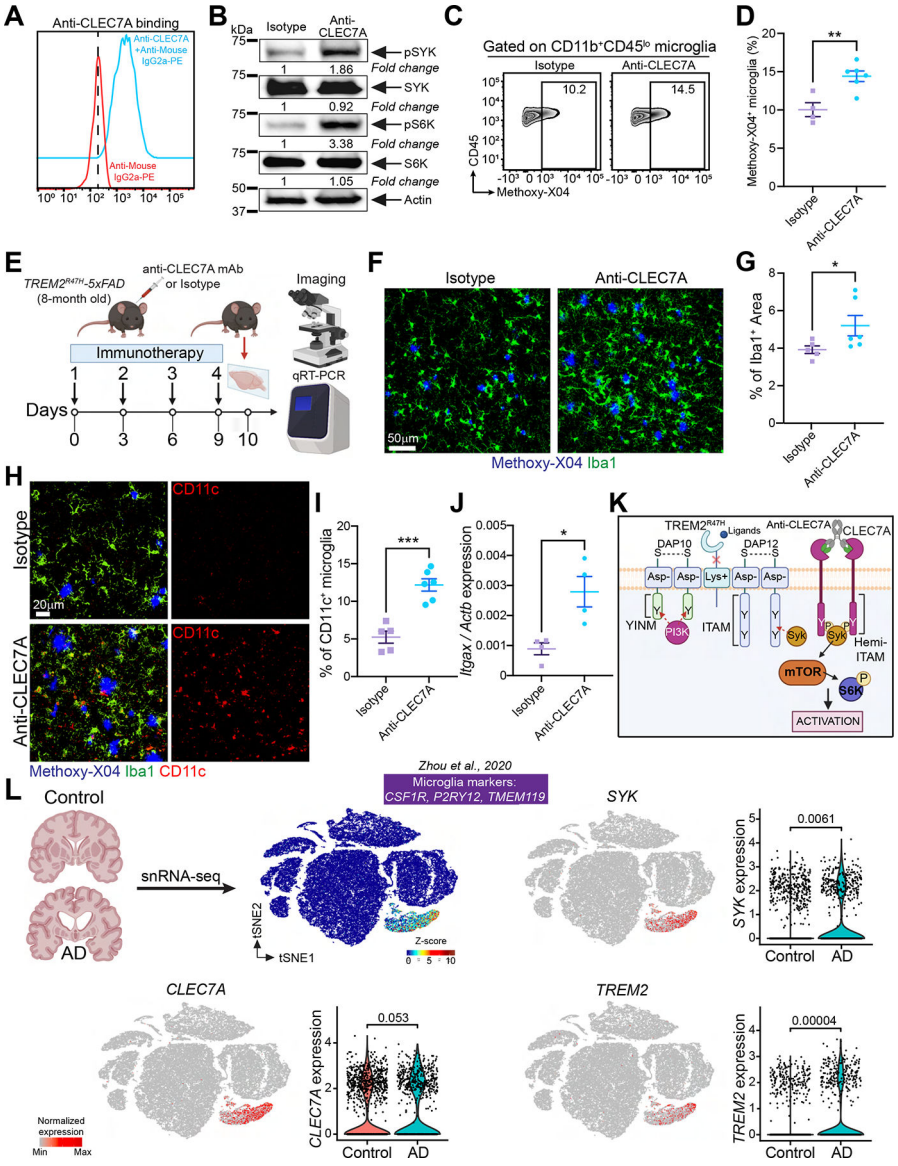

Figure 7. Acute treatment with anti-CLEC7A induces microglial activation in *TREM2^{R47H}-5×FAD* mice

(A) Cultured WT primary microglia from P4 neonates stained with anti-CLEC7A. Cells stained only with secondary Ab served as negative control. Representative of three independent experiments.

(B) Immunoblot of SYK, pSYK, S6K and pS6K on primary microglia treated with either isotype control or anti-CLEC7A. Representative of two independent experiments.

(C) Representative FACS plots of methoxy-X04^{+} microglia from *TREM2^{R47H}-5×FAD* mice, injected ip. with either isotype control or anti-CLEC7A. WT mice served as a negative control to set the methoxy-X04^{+} gate.

(D) Percentage of methoxy-X04^{+} microglia in the tested groups (two independent experiments; n = 4–6 mice/group).

(E) Schematic of the experimental design.

(F) Representative confocal images of Iba1 and methoxy-X04 staining in the cortex of *TREM2*^{R47H}-*5×FAD* mice injected with either isotype control or anti-CLEC7A.
(G) Percentage of Iba1^{+} area in the tested groups. Data points represent the average of two technical repeats (one experiment; n = 5–6 mice/group).
(H) Representative confocal images of methoxy-X04, Iba-1 and CD11c in the cortex of *TREM2*^{R47H}-*5×FAD* mice injected with either isotype control or anti-CLEC7A.
(I) Percentage of CD11c^{+} microglia in the tested groups. Data points represent the average of two technical repeats (one experiment; n = 5–6 mice/group).
(J) *Itgax* mRNA levels assessed by qRT-PCR in whole cortical tissue from *TREM2*^{R47H}-*5×FAD* mice injected with either isotype control or anti-CLEC7A (one experiment; n = 4 mice/group).
(K) Cartoon summarizing the hypothetical pharmacodynamics of anti-CLEC7A in microglia.
(L) tSNE plots of human brain cells from AD patients and control subjects analyzed by snRNA-seq. Expression of SYK, CLEC7A and TREM2 is displayed.
*, P < 0.05, **, P < 0.01, ***, P < 0.001 by two-tailed unpaired Student's t test (D, G, I and J), or Wilcoxon rank-sum test (L). Data are presented as mean ± SEM.
See also Figure S7 in the supplemental information.

KEY RESOURCES TABLE

REAGENT or RESOURCE	SOURCE	IDENTIFIER
Antibodies		
CD45-PE (clone 30-F11)	BioLegend	Cat #103106
CD45-APCCy7 (clone 30-F11)	BioLegend	Cat #103116
CD11b-APC (clone M1/70)	BioLegend	Cat #101212
Ly6C-APCCy7 (clone HK1.4)	BioLegend	Cat #128026
Ly6G-FITC (clone 1A8)	BioLegend	Cat #127606
P2RY12-BV421 (clone S16001E)	BioLegend	Cat #392106
Syk-PE (clone 5F5)	BioLegend	Cat #646004
BrdU-PE (Bu20a)	BioLegend	Cat #339812
anti-CLEC7A antibody-Fc mutated (clone 2A11)	This paper	N/A
anti-human ILT1-Fc mutated (clone 135.5)	In house	(Molgora et al., 2020)
anti-mouse IgG2a-PE	SouthernBiotech	Cat #1080-09
anti-phospho Syk (rabbit monoclonal)	Cell Signaling Technology	Cat #2717
anti-Syk (rabbit monoclonal)	Cell Signaling Technology	Cat #13198
anti-phospho Akt 473 (rabbit monoclonal)	Cell Signaling Technology	Cat #4060
anti-Akt (rabbit monoclonal)	Cell Signaling Technology	Cat #4691
anti-phospho NDRG1 (rabbit polyclonal)	Cell Signaling Technology	Cat #3217
anti-NDRG1 (rabbit polyclonal)	Cell Signaling Technology	Cat #5196
anti-phospho GSK3-β (rabbit polyclonal)	Cell Signaling Technology	Cat #9336
anti-GSK3-β (rabbit monoclonal)	Cell Signaling Technology	Cat #12456
anti-phospho ERK (rabbit polyclonal)	Cell Signaling Technology	Cat #9101
anti-ERK (rabbit monoclonal)	Cell Signaling Technology	Cat #4695
anti-phospho S6K (rabbit monoclonal)	Cell Signaling Technology	Cat #9234
anti-S6K (rabbit polyclonal)	Cell Signaling Technology	Cat #9202
anti-LC3 (rabbit polyclonal)	Cell Signaling Technology	Cat #2775
anti-beta-actin-HRP (mouse monoclonal)	Santa Cruz Biotechnology	Cat #sc-47778 HRP
anti-rabbit IgG, HRP	Cell Signaling Technology	Cat #7074
anti-Iba1 (rabbit monoclonal)	Cell Signaling Technology	Cat #17198
anti-Iba1 (goat polyclonal)	Abcam	Cat #5076
anti-CD68 (rat monoclonal)	BioLegend	Cat #137002
anti-Pu.1 (rabbit monoclonal)	Cell Signaling Technology	Cat #2258
anti-$A\beta_{1-42}$ (rabbit recombinant monoclonal)	Thermo Fisher Scientific	Cat #700254
anti-$A\beta_{1-16}$ (6E10)	BioLegend	Cat #803013
anti-Lamp1 (rat Monoclonal)	BioLegend	Cat #121602
anti-APP (22C11 mouse mAb)	Millipore	Cat #MAB348
anti-LC3-Alexa Fluor® 488 (rabbit monoclonal)	Cell Signaling Technology	Cat #13082
anti-CD11c (rabbit monoclonal)	Cell Signaling Technology	Cat #97585

REAGENT or RESOURCE	SOURCE	IDENTIFIER
anti-CD74-Alexa Fluor® 647 (rat monoclonal)	BioLegend	Cat # 151004
anti-Ki67 (rabbit polyclonal)	Abcam	Cat #15580
anti-ApoE (biotinylated HJ6.3)	Holtzman Lab	(Xiong et al., 2021)
anti-Trem2 (polyclonal sheep)	R&D Systems	Cat #AF1729
anti-Tmem119 (rabbit monoclonal)	Cell Signaling Technology	Cat #90840
anti-Clec7a (rat monoclonal)	InvivoGene	Cat #mabg-mmcl
anti-goat IgG Alexa-Fluor®488 (donkey polyclonal)	Abcam	Cat #150129
anti-rabbit IgG Alexa Fluor® 555 (donkey polyclonal	Abcam	Cat #150074
anti-goat IgG Alexa Fluor® 647 (donkey polyclonal)	Abcam	Cat #150131
anti-rabbit IgG Alexa Fluor® 647 (goat recombinant polyclonal)	Invitrogen	Cat #A-21244
anti-rat IgG Alexa Fluor®647 (chicken polyclonal)	Invitrogen	Cat # A-21472
anti-sheep IgG Alexa Fluor® 555 (donkey polyclonal)	Abcam	Cat #150178
Streptavidin-Alexa Fluor® 647	BioLegend	Cat #405237
goat F(ab')2 anti-mouse IgG(H+L) (polyclonal)	SouthernBiotech	Cat #1032–01
Bacterial and virus strains		
pFUSEmIgG2A-Fc1 vector expressing a DNA fragment encoding heavy chain variable and CH1 regions of anti-CLEC7A antibody (clone 2A11)	This paper	N/A
Fc-null pFUSE-mIgG2A-Fc1 vector expressing a DNA fragment encoding the light chain of anti-CLEC7A antibody (clone 2A11)	This paper	N/A
Chemicals, peptides, and recombinant proteins		
MitoTracker Green	Invitrogen	Cat #M7514
Aqua fluorescent reactive dye	Life technologies	Cat #L34966
Methoxy-X04	Tocris Biosciences	Cat #4920
Propidium Iodide	Invitrogen	Cat # P1304MP
BrdU	Invitrogen	Cat # B23151
β-amyloid (1–42) peptide - unlabeled	Anaspec	Cat #AS-20276
SuperSignal West Pico PLUS Chemiluminescent substrate	Thermo Fisher Scientific	Cat #34579
TO-PRO-3 iodide	Life Technologies	Cat #T3605
BAY61–3606	Selleckchem	Cat #S7006
SB216763	Tocris Biosciences	Cat #1616
Critical commercial assays		
Foxp3/Transcription Factor Staining Buffer Set	Invitrogen	Cat #00-5523-00
BD Pharmingen BrdU Flow Kit	BD Biosciences	Cat #557892
pHRodo iFL Labeling kit	Invitrogen	Cat #P36014
miRNeasy Mini Kit	QIAGEN	Cat #217084
High-Capacity cDNA Reverse Transcription Kit	Applied Biosystems	Cat #4368814
SYBR Green real-time PCR master mix	Applied Biosystems	Cat # 4309155
Deposited data		
10x Single Cell RNA-seq: $Syk^{fl/fl}$, $Syk^{fl/fl}$-$Cx3cr1^{CreERT2}$, $Syk^{fl/fl}$-5×FAD, 5×FAD transgenic mice, $Dap12^{K\Delta Y75}$-5×FAD and $Trem2^{-/-}$-5×FAD	This paper	GSE210258
Experimental models: Cell lines		

REAGENT or RESOURCE	SOURCE	IDENTIFIER
Primary murine microglia	This paper	N/A
Primary murine BMDM	This paper	N/A
Expi293F Cells	Thermo Fisher Scientific	Cat #A14527
Experimental models: Organisms/strains		
C57BL6/J	Jackson Laboratory	Cat #000664
5×FAD transgenic mice	Jackson Laboratory	Cat #034840-JAX
$Cx3cr1^{Cre}$	Jackson Laboratory	Cat #025524
$Cx3cr1^{CreERT2}$	Jackson Laboratory	Cat #021160
$Syk^{fl/fl}$	Jackson Laboratory	Cat #017309
$Syk^{fl/fl}$-5×FAD	This paper	N/A
$Syk^{fl/fl}$-$Cx3cr1^{Cre}$	This paper	N/A
$Syk^{fl/fl}$-$Cx3cr1^{CreERT2}$	This paper	N/A
$Syk^{fl/fl}$-$Cx3cr1^{CreERT2}$-5×FAD	This paper	N/A
$Dap10^{-/-}$	In house	(Gilfillan et al., 2002)
$Dap12^{K\Delta Y75}$	In house	(Tomasello et al., 2000)
$Dap12^{K\Delta Y75}$-5×FAD	This paper	N/A
$Trem2^{-/-}$	In house	(Wang et al., 2015)
$Trem2^{-/-}$-5×FAD	In house	(Wang et al., 2015)
$Trem2^{R47H}$-5×FAD	In house	(Song et al., 2018)
Oligonucleotides		
Itgax qPCR FW: CTGGATAGCCTTTCTTCTGCTG RV: GCACACTGTGTCCGAACTCA	This paper	N/A
Actin qPCR FW: GGAGGGGGTTGAGGTGTT RV: TGTGCACTTTTATTGGTCTCAA	This paper	N/A
Recombinant DNA		
anti-CLEC7A antibody-Fc mutated plasmids (clone 2A11)	This paper	N/A
anti-human ILT1-Fc mutated plasmids (clone 135.5)	In house	(Molgora et al., 2020)
Software and algorithms		
MATLAB	MathWorks	N/A
ImageJ	National Institutes of Health	N/A
Bio-Rad ChemiDoc MP imaging system	Bio-Rad Laboratories	N/A
AMT Image Capture Engine V602 software	Advanced Microscopy Techniques	N/A
FlowJo	FlowJo	www.flowjo.com/
Imaris 7.7	Bitplane	N/A
Cell Ranger Software Suite (v6.0.0)	10x Genomics	N/A
Seurat (v4.0)	(Hao et al., 2021)	N/A
R (v4.1.0)	R Core Team (2017). R: A language and	N/A

REAGENT or RESOURCE	SOURCE	IDENTIFIER
	environment for statistical computing. R Foundation for Statistical Computing, Vienna, Austria. URL http://www.R-project.org/.	
BBrowser v2.7.5	BioTuring Inc.	www.bioturing.com/bbrowser
slingshot (v2.1.0)	(Street et al., 2018)	N/A
tradeSeq (v1.6)	(Van den Berge et al., 2020)	N/A
GraphPad Prism 9	GraphPad	www.graphpad.com
Other		
TAM Diet (500, 2016)	Envigo	TD.130857